

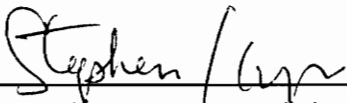
High Temperature Flow Behavior of Titanium Aluminide Intermetallic Matrix Composites

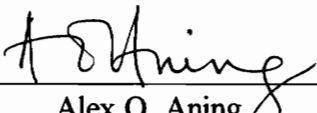
by

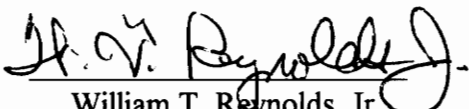
Judson S. Marte

Thesis submitted to the faculty of the
Virginia Polytechnic Institute and State University
in partial fulfillment of the requirements for the degree of
MASTER OF SCIENCE
in
Materials Science and Engineering

APPROVED:


Stephen L. Kampe, chair


Alex O. Aning


William T. Reynolds, Jr.

April, 1996
Blacksburg, VA

Keywords: Al_3Ti , Titanium Aluminides, Intermetallic Matrix Composite, Reaction Synthesis, Dispersion Strengthened Composite, Constitutive Equation, Zener-Hollomon Parameter.

c.2

LD
5655
V855
1996
M3758
c.2

HIGH TEMPERATURE FLOW BEHAVIOR OF TITANIUM ALUMINIDE INTERMETALLIC MATRIX COMPOSITES

by

Judson S. Marte

Committee Chairman: Stephen L. Kampe
Materials Science and Engineering

(ABSTRACT)

Al_3Ti , Al_5CuTi_2 , and $\text{Al}_{66}\text{Mn}_{11}\text{Ti}_{23}$ intermetallic matrices reinforced with 30, 40, and 50 volume % TiB_2 have been produced by XD™ processing and densified into bulk form by powder metallurgy techniques. The compressive flow behavior of the Al_3Ti and Al_5CuTi_2 composites have been evaluated at temperatures ranging from 1000°C to 1200°C and strain rates of 0.0001 and 0.001 sec^{-1} . The results have been analyzed by a correlation to the resulting microstructure, especially with regards to the intermetallic matrix composition, TiB_2 size, and interparticle spacing. The results of these analyses are applied to a constitutive equation based upon the flow stress equation.

It has been shown that at in this temperature regime, all deformation occurs within the intermetallic matrix. This is substantiated by the lack of TiB_2 -dependent behavior with variations in volume percentage of reinforcement. In all cases, the composites are readily deformed at relatively low loads. The average strain-rate sensitivity values were 0.349 for the Al_3Ti -based composites, and 0.247 for the Al_5CuTi_2 variants. The average activation

energies were calculated to be 485 kJ/mol and 920 kJ/mol for the Al_3Ti - and Al_5CuTi_2 -matrices, respectively. The structure constant was calculated based upon these values. The Zener-Hollomon parameter was used to plot the flow stress along lines of constant temperature and strain rate, and serves as one type of constitutive equation. In addition, the flow stress was evaluated as a function of the strain rate and temperature. These models were found to provide adequate correlation to the measured flow behavior.

Acknowledgements

The author wishes to thank his advisor, Dr. S.L. Kampe, for his direction and support and Drs. A.O. Aning and W.T. Reynolds, Jr. for their enthusiasm and guidance. He would also like to acknowledge the financial support of the MSE department of Virginia Tech, Tony Zahrah of MATSYS, Inc., and Steve Fishman of the Office of Naval Research. In addition, the author would like to acknowledge the assistance of Ken Killian and Drs. Richard Everitt and William Lechter of the Naval Research Laboratory in Washington, D.C. for their assistance in the saga of the HIP, and Dr. Andrew Weresczak and Timothy Kirkland at Oak Ridge National Lab's High Temperature Materials Lab User's Center for their assistance with the compression testing equipment.

Special thanks are due to the students of the Materials Science and Engineering department who were very helpful, especially: Jeff Clinedist, Jason Hansen, Raphael Martin and Thobeka Pete. Sincerest thanks also go to the staff of the department for their unfaltering patience and ability to rally financial support, especially: Harry Dudley, John Pataki, Amy Hill, Jan Doran and Dr. Ronald Gordon. In addition, I would like to thank all of my friends at Virginia Tech not listed in any of the previous acknowledgements: Heidi Allison, Robert Carter, James Clark, Curt Crowder, Levon Fattal, Rebecca Herrmann, Joel Lee, Michael Stawovy, Kimberly Walton, Jesse Weissmann and the many the others whom I've had the privilege to come into contact with while at Virginia Tech.

Finally, I would like to thank my family, Charles, Edith, Ryan and Spencer Marte, without their moral support, I would never have had the motivation to pursue graduate research.

TABLE OF CONTENTS

Abstract	ii
Acknowledgements	iv
Table of Contents	vi
List of Figures	vii
List of Tables	x
0. Objective and summary of research	xi
1. Introduction	1
1.1. Al-Ti Intermetallics as Matrices	2
1.2. <i>In-situ</i> Reinforcement Strategy	5
1.2.1. Constitutional <i>in-situ</i> Processing Techniques	7
1.2.2. Morphological <i>in-situ</i> Processing of metal matrix composites	9
1.3. Summary	11
2. Experimental Procedures	12
2.1. Foreground	12
2.2. Reaction Synthesis	13
2.3. Comminution of IMC Sponges	17
2.4. Consolidation of IMC's	20
2.5. Compression Testing	22
2.6. Metallographic Preparation	25
2.6.1. TiB ₂ crystal size analysis	26
2.6.2. TiB ₂ crystal spacing analysis	26
2.6.3 X-ray Diffraction Analysis	27
3. Experimental Results	28
3.1. Reaction Synthesis	28
3.1.1. Formulations and Conditions	28
3.1.2. Qualitative Description of the Reaction Synthesis	29
3.1.2.1. Effect of volume % TiB ₂ on the reaction	30
3.1.2.2. Effect of the matrix composition on the reaction	31
3.1.2.3. Effect of the atmosphere on the reaction	31
3.2. Microstructural Analysis	32
3.2.1. Matrix Microstructures	32
3.2.1.1. Effects of Matrix Composition on Microstructure	32

3.2.1.2. X-ray Diffraction Analysis of As-tested Samples	36
3.2.1.2.1. XRD of Al ₃ Ti matrix composites	36
3.2.1.2.2. XRD of Al ₃ CuTi ₂ matrix composites	37
3.2.2. Analysis of Dispersed TiB ₂ Particulates	38
3.3. Mechanical Behavior	43
3.3.1. General	43
3.3.2. Development of Constitutive Equations	45
3.3.2.2. The Strain-rate Sensitivity, m	46
3.3.2.3. The Activation Energy, Q	50
3.3.2.4. Structure Constant, A	54
4. Discussion	56
4.1. Correlation of Microstructure to Mechanical Behavior	56
4.1.1. Effects of TiB ₂ reinforcement	56
4.1.1.1. Effect of Volume % on TiB ₂ Size	56
4.1.1.2. Volume % TiB ₂ Reinforcement	58
4.1.1.3. TiB ₂ particle size and interparticle spacing	61
4.1.1.4. Models of Dispersion Strengthening	61
4.1.2. Effect of the matrix composition on the mechanical behavior of the composites	62
4.1.2.1. Matrix Composition and Homologous Temperature	62
4.2. Development of Constitutive Equations	65
4.2.1. The Zener-Hollomon Parameter	65
4.2.2. Constitutive Flow Stress Equations	68
4.3. Future Work and Potential Applications	77
4.3.1. Application to other intermetallic matrix composites	77
4.3.2. Codeformation Processing	77
4.4. Summary and Conclusions	78
4.4.1. Summary	78
4.4.2. Conclusions	79
References	81
Vita	84

LIST OF FIGURES

Figure #	Title	Page
Figure 1	The Phase Diagram of the Ti-Al System showing the intermetallic phases Ti_3Al , $TiAl$ and Al_3Ti . ⁴⁹	2
Figure 2	Unit Cells of Al_3Ti -based compounds with $L1_2$ (a), and $D022$ (b). The reciprocal lattice corresponding to (b) is shown in (c). The open and solid circles represent primary and superlattice reflections, respectively. ⁴⁵	4
Figure 3	A diagram which pictographically displays the experimental procedures.	13
Figure 4	Mechanical sieve analysis of particle size distribution of Al_3Ti , Al_5CuTi_2 , and $Al_{66}Mn_{11}Ti_{23}$ reinforced with 30 volume % TiB_2 .	18
Figure 5	Mechanical sieve analysis of particle size distribution of Al_3Ti , Al_5CuTi_2 , and $Al_{66}Mn_{11}Ti_{23}$ reinforced with 40 volume % TiB_2 .	19
Figure 6	Mechanical sieve analysis of particle size distribution of Al_3Ti , Al_5CuTi_2 , and $Al_{66}Mn_{11}Ti_{23}$ reinforced with 50 volume % TiB_2 .	19
Figure 7	Titanium tubing used in encapsulation of the IMCs. (a) the pre-reacted powder mixture, (b) an as-reacted IMC sponge, (c) titanium tube cut to length, (d) a crimped and welded titanium can.	21
Figure 8	Results of HIP consolidation at $1300^\circ C$ and 205 MPa for 2 hours. No visible pores are observed in this micrograph.	22
Figure 9	A typical micrograph of the as-polished intermetallic matrix composites. Note the presence of TiB_2 crystals throughout.	34
Figure 10	Micrograph of the basketweave structure observed in $Al_5CuTi_2 + 30$ and 40 volume % TiB_2 after HIP'ing at $1300^\circ C$ and 205 MPa for 2 hours.	35
Figure 11	Multiphase regions appear as different shades of gray in the matrix portion of the composite in a sample of $Al_3Ti + 30$ volume % TiB_2 .	35
Figure 12	Multiphase regions appear as different shades of gray in the matrix portion of the composite in a sample of $Al_5CuTi_2 + 30$ volume % TiB_2 .	36
Figure 13	An X-ray Diffraction peak pattern from $Al_3Ti + 40$ volume % TiB_2 . This pattern is typical of all of the Al_3Ti matrix compositions.	37
Figure 14	An x-ray diffraction pattern from $Al_5CuTi_2 + 40$ volume % TiB_2 . This pattern is typical of the Al_5CuTi_2 -matrix composites.	38
Figure 15	Average particle size of TiB_2 reinforcements in the as-reacted intermetallic matrix composites reacted under a partial pressure of argon.	41
Figure 16	Average aspect ratio of TiB_2 particulate reinforcements in the as-reacted intermetallic matrix composites reacted under a partial pressure of argon.	42
Figure 17	Average interparticle spacing of the TiB_2 reinforcements in the as-HIP'd intermetallic matrix composites originally reacted under a partial pressure of argon.	42
Figure 18	A typical True Stress vs. True Strain curve. This particular curve is from a compression test. The sample in this case was $Al_3Ti + 30$ volume % TiB_2 at $1100^\circ C$ and 0.001 sec^{-1} .	44
Figure 19	Plot of true peak stress versus strain rate on a log scale for each composites at $1000^\circ C$. The slope of the trace of a line drawn between the points for each composite is equal to that composite's strain rate sensitivity, m . Circled points were not used in the actual calculation of the strain-rate sensitivity.	47

Figure 20	Plot of true peak stress versus strain rate on a log scale for each composites at 1100°C. The slope of the trace of a line drawn between the points for each composite is equal to that composite's strain rate sensitivity, m . Circled points were not used in the actual calculation of the strain-rate sensitivity.	48
Figure 21	Plot of true peak stress versus strain rate on a log scale for each composites at 1200°C. The slope of the trace of a line drawn between the points for each composite is equal to that composite's strain rate sensitivity, m .	49
Figure 22	Plot of the true peak stress versus the inverse temperature on a log-linear scale for each of the composites at 0.0001s^{-1} . The slope of the trace of a trend line for each composition is proportional to that composite's activation energy.	52
Figure 23	Plot of the true peak stress versus the inverse temperature on a log-linear scale for each of the composites at 0.001s^{-1} . The slope of the trace of a trend line for each composition is proportional to that composite's activation energy. The circled points represent those not used in the calculations for activation energy due to temperature measurement errors.	53
Figure 24	The TiB_2 equivalent particle diameter as a function of the adiabatic temperature.	58
Figure 25	A comparison of flow stress as a function of volume % TiB_2 reinforcement at 1000°C.	59
Figure 26	A comparison of flow stress as a function of volume % TiB_2 reinforcement at 1100°C.	60
Figure 27	A comparison of flow stress as a function of volume % TiB_2 reinforcement at 1200°C.	60
Figure 26	A comparison of flow stress as a function of interparticle spacing.	63
Figure 27	A plot of the average flow stress as a function of the homologous temperature.	65
Figure 28	The peak flow stress as a function of the Zener-Hollomon Parameter.	67
Figure 29	A plot of the flow stress as a function of the temperature and strain rate for $\text{Al}_3\text{Ti} + 30$ volume % TiB_2 .	71
Figure 30	A plot of the flow stress as a function of the temperature and strain rate for $\text{Al}_3\text{Ti} + 40$ volume % TiB_2 . It correlates well to the measured flow stresses.	72
Figure 31	A plot of the flow stress as a function of the temperature and strain rate for $\text{Al}_3\text{Ti} + 50$ volume % TiB_2 .	73
Figure 32	A plot of the flow stress as a function of the temperature and strain rate for $\text{Al}_5\text{CuTi}_2 + 30$ volume % TiB_2 .	74
Figure 33	A plot of the flow stress as a function of the temperature and strain rate for $\text{Al}_5\text{CuTi}_2 + 40$ volume % TiB_2 .	75
Figure 34	A plot of the flow stress as a function of the temperature and strain rate for $\text{Al}_5\text{CuTi}_2 + 50$ volume % TiB_2 .	76

LIST OF TABLES

Table #	Table Title	Page
Table I	Melting temperatures of Ti-Al IMCs and Ti alloys.	5
Table II	Physico-chemical classification of SHS reaction mechanisms for a two component system.	8
Table III	Nominal volume percentage composition of intermetallic matrix composites.	14
Table IV	Weight percentages used to formulate intermetallic matrices and reinforcements for IMCs.	15
Table V	Weight percentages of matrix and reinforcement materials used to formulate Al ₃ Ti-based IMCs.	16
Table VI	Different Conditions Used for the synthesis of Al ₃ Ti-based IMCs and their labels.	29
Table VII	TiB ₂ average particle size and 95% confidence intervals from manual measurements	40
Table VIII	A comparison of the measured interparticle spacing and the as-calculated interparticle spacing	43
Table IX	The true plastic stress peaks and the true plastic strains at which those peaks occur (after application of a correction factor).	45
Table X	Strain-rate sensitivity values for each composite at each test temperature.	50
Table XI	Activation energy values for each composite at each strain-rate.	54
Table XII	The structure constant as calculated for each composite.	55
Table XII	The homologous temperature for each composite matrix at the specified test temperatures.	64
Table XIV	The structure factors, strain-rate sensitivities, and activation energies utilized in the flow stress equation-based constitutive equations.	69
Table XV	A list of potential intermetallic matrices and reinforcements.	77

0. OBJECTIVE AND SUMMARY OF APPROACH

The objective of the research effort described herein is to characterize fundamental structure property relationships and phenomenological-based constitutive equations to model the high temperature flow behavior of a series of titanium aluminide intermetallic matrix composites. This information is important and necessary for the eventual determination of specific conditions for the successful and efficient processing of these materials by thermo-mechanical means.

To accomplish these objectives, a series of intermetallic matrix composites (IMCs) comprised of matrices based upon Al_3Ti systems reinforced with a discontinuous dispersion of titanium diboride (TiB_2) have been produced using reaction synthesis techniques. The alloys have been subsequently consolidated into bulk form using conventional powder metallurgy (P/M) methods. The samples were evaluated in compression, and flow stresses were measured at high temperatures at a variety of strain rates. Both matrix and reinforcement percentage have been systematically varied to assess their relative influence on the flow stress and strain-rate sensitivity. The peak true stress was used to develop behavioral models based upon matrix composition and volume percentage reinforcement. The data was analyzed using various approaches which have been advanced to describe high temperature flow.

A summary of the specific goals of the project include:

- determining the flow stress of the IMC's at elevated temperatures,
- calculating the activation energy for deformation and the strain rate sensitivity of the flow stress of the IMC's,
- characterizing the composite microstructure in terms of the size, aspect ratio and spacing of the TiB_2 reinforcement,
- correlating the mechanical behavior of the IMC to the aforementioned microstructural features, and intermetallic matrix, including the influence of temperature on that behavior, and
- Developing a constitutive model for the compressive flow of these materials at a series of temperatures and strain rates.

1.0 INTRODUCTION

Intermetallic based alloys and intermetallic matrix composites (IMCs) have been the focus of numerous studies for their potential as low-density alternatives to the heavier nickel- and iron-based superalloys in high temperature applications¹⁻¹². Intermetallics can be defined as ordered alloy phases formed between two or more metallic elements, where an alloy phase is ordered if two or more sublattices are required to describe its atomic structure.¹² These materials offer an attractive combination of strength, high melting temperature, and potentially good oxidation resistance. Further, atomic diffusion and dislocation motion are more difficult than in conventional alloys since additional constraints are imposed to maintain the ordered structure. An ordered structure restricts dislocation motion by forcing most, or all motion to occur via superdislocations which require much higher stresses. The ordered structure also reduces the diffusion rates, since atomic motion tends to occur in pairs to maintain the ordered nature of the lattice. Several studies have linked these features to the potential for excellent elevated temperature strength retention and creep behavior^{13, 14} since resistance to both dislocation- and diffusion-based mechanisms are simultaneously addressed.

However, offsetting these favorable elevated temperature attributes is a lack of room temperature ductility, toughness, and damage tolerance, thereby restricting their acceptance for most current high temperature structural applications. In general,

intermetallic alloys are extremely brittle at low to moderate temperatures, including room temperature. Macroscopically, their room temperature fracture behavior is not unlike that of traditional ceramic materials.

1.1. Ti-Al Intermetallics

The low density and strength capabilities of the intermetallics in the Ti-Al system have generated significant interest in recent years. The Ti-Al system contains three stable intermetallic compounds, Ti_3Al , $TiAl$, and Al_3Ti , as shown in Figure 1.

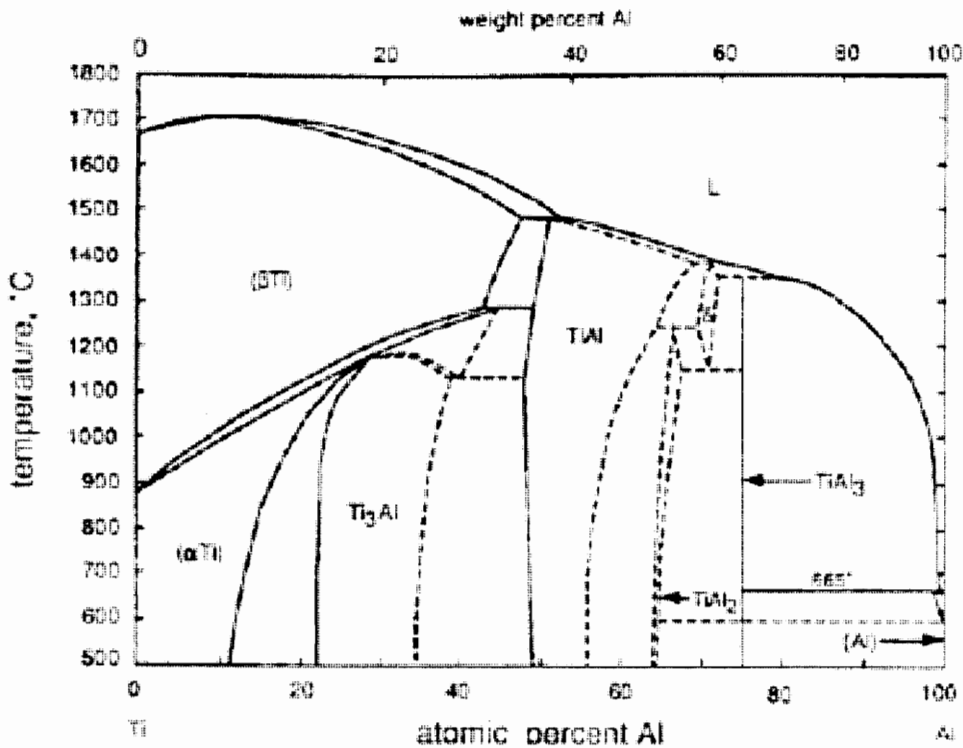


Figure 1: The Phase Diagram of the Ti-Al System showing the intermetallic phases Ti_3Al , $TiAl$ and Al_3Ti .¹⁴

Most research has been focused on either Ti_3Al (α_2), TiAl (γ) or a combination of the two (i.e., "near- γ ") because of the potential for near-term application of these systems. The Al_3Ti compound has, in general, been overlooked because of its severe brittleness at ambient temperatures, even relative to Ti_3Al and TiAl . Most investigations of the TiAl - and Al_3Ti -based intermetallics have been conducted in an attempt to overcome their lack of room temperature ductility. In the latter regard, the approach most generally taken is to transform the crystal structure from tetragonal DO_{22} to the cubic L1_2 by increasing the lattice parameter in the c-direction by selective substitutional alloying. The transformation of the crystal structure is shown in Figure 2. The L1_2 cubic system gives the required five nearly-equivalent slip systems to satisfy the Von Mises Criterion thus improving the ductility somewhat. Although many metals do generate the desired cubic microstructure, only Cr, Fe and Mn alloy-modified structures have been shown to improve compressive ductility significantly.¹⁵⁻²⁰ However, for this study the significant benefit of this previous research does not lie in the enhanced ductility at room temperature. Instead, the effect of certain alloying additions on the melting temperature of the Al_3Ti is of interest, since this will likely influence its flow behavior at elevated temperatures. The ability of certain elements to depress the melting temperature of the original Al_3Ti is shown in Table I. Monolithic Al_3Ti has a ductile-to-brittle transition temperature of approximately 800°C.

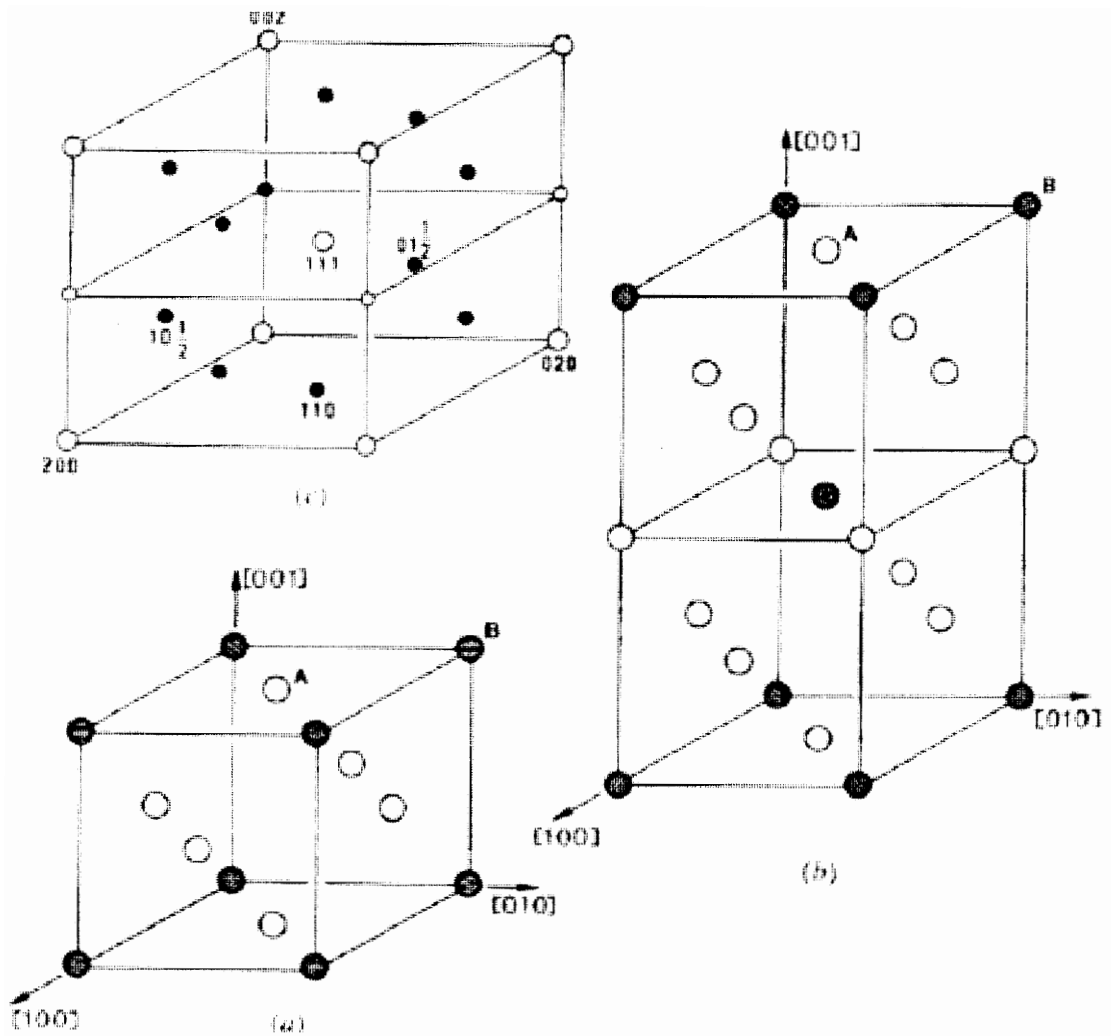


Figure 2: Unit Cells of Al_3Ti -based compounds with $L1_2$ (a), and $D0_{22}$ (b). The reciprocal lattice corresponding to (b) is shown in (c). The open and solid circles represent primary and superlattice reflections, respectively.²¹

Table I: Melting temperatures of Ti-Al IMCs and Ti alloys.

Compound	T _{melt} (°C)
Al ₃ Ti	1367 ¹
Al ₅ CuTi ₂	1350 ²
Al ₆₆ Mn ₁₁ Ti ₂₃	1339 ³
Al ₆₇ Mn ₈ Ti ₂₅	1402 ⁴
TiAl	1460 ⁵
C.P. Ti	1668 ¹
Ti-6Al-4V	1672 ⁶

1. I Barin, et.al., *Thermochemical Data of Pure Substances, 2nd ed.*, VCH, Weinheim, Germany, 1989.²²
2. J. Tarnacki and Y-W. Kim, "A Study of Rapidly Solidified Al₃Ti Intermetallics with Alloying Additions", *Scr Met*, vol. 22, pp. 329-34, (1988).²³
3. as measured using DTA.
4. X. Chen, X. Wu, W.L. Fang, S. Chen & G. Hu, "The Role of Hot-working on the Microstructure and Mechanical Properties of the L12-type Mn Modified Al₃Ti Alloy", *Mat Sci Eng*, vol. A153, pp. 370-6, (1992).¹⁹
5. I. Barin, *Thermochemical Properties of Inorganic Substances by I. Barin and O. Knacke*, Springer-Verlag, Berlin, Germany, (1973).²⁴
6. D.A. Porter and K.E. Easterling, *Phase Transformations in Metals and Alloys*, Van Nostrand Reinhold (International), p. 366, (1988).²⁵

1.2. *In-situ* Intermetallic-Matrix Composites

In this study, the titanium aluminide matrix composites will be synthesized utilizing an in-situ processing technique. Interfacial strength and thermochemical stability are imperative to the high-temperature strength, stability and modulus of an intermetallic matrix composite. An *in-situ* reinforced composite can be defined as one in which the

reinforcing phase is formed directly within the matrix of the composite during synthesis. There are many advantages to developing an *in-situ* reinforcing scheme, among them clean interfaces, economical processing and safety. The most significant advantage from this study's point of view is the development of clean interfaces. *In-situ* processing results in composites that are essentially free of environmental contamination originating from environmental exposure during handling or processing. Usually, the interfaces are chemically compatible with the matrix because they were formed through a thermodynamically-favored reaction with the matrix materials. The generation of *in-situ* reinforcements also eliminates the safety problems associated with the handling of fine metal or ceramic particles. Because of the elimination of coating techniques and handling problems, the potential production cost and environmental concerns are diminished.

In-situ composite processing can be categorized into two major classes. Strategies in which the reinforcement is chemically synthesized *in-situ* are referred to as constitutional techniques. Those that lead to *in-situ* reinforcement shape evolution are classified as morphological techniques.

1.2.1. Constitutional *in-situ* Processing Techniques

Constitutional processing can be defined as the synthesis of a composite in which the reinforcement is directly created within the matrix. There are several methods by which this formation can occur. Examples include:

- Liquid-gas reactions in which a gas is injected into a molten metal to react with the metal, forming the reinforcing phase;
- Solid-gas (reactive plasma) reactions using the high thermal energy of a plasma to precipitate a solid from a gas;
- Liquid-solid processing (reaction synthesis) using high temperatures to initiate a self-sustaining exothermic reaction in which a reinforcing phase precipitates in the matrix solvent via diffusion of its components.

The XD™ process, an *in-situ* reaction synthesis-based technique developed by Martin-Marietta, will be utilized in this study to create the discontinuously-reinforced intermetallic matrix composite. This process is of the liquid-solid processing variety and relies in part upon principles established for self-propagating high-temperature synthesis (SHS). Unlike SHS, XD™ allows for the synthesis of multi-component systems (e.g., $\text{Al}+\text{Ti}+\text{B} = \text{Al}_3\text{Ti} + \text{TiB}_2$, etc.) Elemental powders of the desired composite constituents are mixed, compacted and ignited to begin the exothermic reaction. Exothermicity and reaction-self-sustenance occur as the thermodynamically-favored ceramic particulates are formed within the protective metallic matrix "solvent". The reaction is completed almost instantaneously and a dispersion of fine ceramic precipitates is formed throughout the

metallic matrix. The requirements for such a reaction to occur are described in detail by Subrahmanyam and Vijakumar.²⁶

Merzhanov, et. al. established a classification of SHS reactions for binary systems which can be qualitatively applied to XD™ processing as well. This system of classification is based on the adiabatic temperature, melting temperature and boiling temperature of the constituents, Table II.

Table II: Physico-chemical classification of SHS reaction mechanisms for a two component system.²⁷

Relation between T_{ad} , T_m and T_b	Characteristics of the System	Examples
$T_{ad} < T_{ib}$ $i=1,2$	Ideal gas free combustion occurs if $[P(T_{ad})/P_0] \rightarrow 0$	$Ti+2B=TiB_2$ gasless reaction only at high pressure $Mo+B=MoB$ gasless reaction even in high vacuum
$T_{im} < T_{ad} < T_{ib}$ $i=1,2$	Both components in liquid state	$Ni+Al=NiAl$
$T_{1m} < T_{ad} < T_{2m}$	Solid+liquid reaction, highest propagation velocity	$Ti+C=TiC$
$T_{ad} < T_{im}$ $i=1,2$	Both components in solid state, lowest combustion velocity, difficult combustion	$2Ta+C=Ta_2C$
$T_{ib} < T_{ad} < T_{2b}$	One component in the gaseous state and the other in condensed state, widely used process	Formation of nitrides, hydrides, sulfides, selenides, phosphides, etc.
$T_{ad} > T_{ib}$ $i=1,2$	Both reactants in gas state and solid product	Very few systems studied, $Mg+S$

The adiabatic temperature, T_{ad} , is used to describe the exothermicity of the system and is used as an empirical guide to decide whether a self-propagating reaction will occur according to the following guidelines:

- $T_{ad} < 1500$ K, combustion does not occur;
- 1500 K $< T_{ad} < 2500$ K, combustion cannot propagate but can be ignited;
- $T_{ad} > 2500$ K, self-sustaining combustion.

Martin²⁸ adapted a modification of Merzhanov's idea to accommodate the solvent phase present in the XDTM process. Martin assumed that the adiabatic temperature, T_{ad} , is calculated under the assumption that all heat generated is used to increase the temperature of the final products, incorporating the XDTM process' solvent phase in the calculation. Thus the calculated adiabatic temperature is the highest temperature the system can reach, since it assumes no heat losses to the surroundings.

1.2.2. Morphological *in-situ* Processing of metal matrix composites

During morphological *in-situ* processes, the composite's microstructure is formed through unconventional processing of an otherwise "conventional" alloy in which the

primary effect of the processing is seen in the shape and orientation of the reinforcement phase. Examples of morphological *in-situ* techniques are:

- Directional solidification, in which an aligned, continuously-reinforced composite is formed via unidirectional solidification of a liquid eutectic alloy.
- Lanxide processes such as the DIMOX® (directional metal oxidation) or the PRIMEX® processes, used to produce near-net-shaped metal matrix composites.
- Deformation processes, in which a desired composite microstructure is formed via mechanical deformation techniques.

One future application of the present research will attempt to use the high-temperature deformability characteristics of an IMC "reinforcement" to achieve in-situ elongation within a metal matrix. This was partially demonstrated by the work of Pete and Martin,²⁸ where extrusions of IMC-reinforced titanium matrix composites were produced at elevated temperatures (1066°C). These extrusions did not exhibit fully commensurate deformation between matrix and the intermetallic matrix composite. It was concluded that the titanium matrices (Commercially Pure Ti and Ti-6Al-4V) did not impart enough stress onto the near- γ TiAl/TiB₂ IMC particles to deform them. A major objective of this study is to address this problem in a more fundamental manner by measuring flow behavior of the IMC as a function of temperature, strain-rate and composition such that the processing conditions can be more efficiently determined. It is expected that if the homologous temperature (i.e., T/T_{melt}) of the reinforcing phase could be decreased (e.g., by alloying of

Al₃Ti), then the titanium alloy matrix would transmit enough stress to effectively deform the IMC.

1.3. Summary

The high temperature mechanical flow behavior of a series of τ -Al₃Ti-based matrix composites produced via reaction synthesis techniques will be characterized. The following variables will be investigated

- Temperature, i.e., at $T \approx 1000^\circ\text{-}1200^\circ\text{C}$,
- Strain-rate, for $\dot{\epsilon} \approx 10^{-4}\text{-}10^{-3} \text{ sec}^{-1}$
- Matrix composition and its effect on $T_{\text{homologous}}$, and
- Volume percentage of the discontinuous, ceramic reinforcement phase.

2. EXPERIMENTAL PROCEDURES

2.1. Foreground

The Al₃Ti-based IMCs are synthesized from elemental powders and prepared for testing by communitively reducing the as-reacted sponge powder size. The resulting IMC powders are then consolidated via hot isostatic pressing (HIP) into right cylinders and mechanically tested in compression at elevated temperatures at a series of strain-rates. This is shown diagrammatically in Figure 3. A microstructural analysis was performed on the samples to determine the equivalent diameter, aspect ratio and interparticle spacing of the dispersed reinforcing phase.

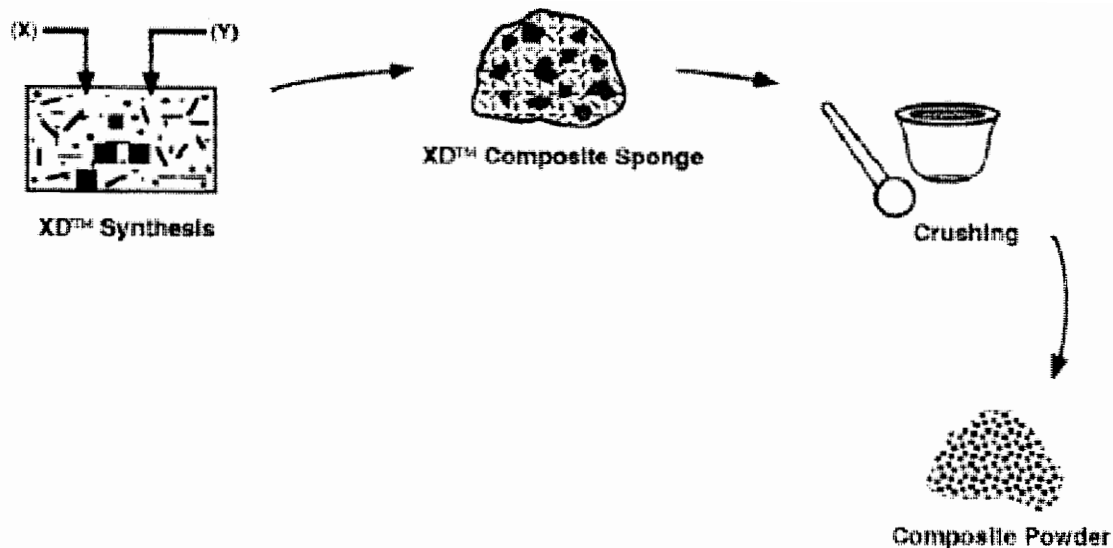


Figure 3: A diagram which pictographically displays the experimental procedures.³⁰

2.2. Reaction Synthesis Processing

Several intermetallic matrix composites with varying matrices and volume percentages of TiB_2 reinforcement were made using XDTM synthesis. All intermetallic composite matrices investigated are based upon the Al_3Ti stoichiometry. The composition of the fifteen IMC matrices created and their designations are presented in Table III.

Elemental powders of titanium, aluminum, copper, manganese and boron were used as precursors to the reaction. Commercially-pure (C.P.) titanium was obtained in a size range of -100 mesh ($\leq 149 \mu\text{m}$) from Micron Metals, Inc. (Salt Lake City, UT)

produced by the hydride/dehydride process (99.95% purity). The aluminum powder was obtained in a size range of -325 mesh ($\leq 44.5 \mu\text{m}$, 99.9% purity) from Atlantic Equipment Engineers (Bergenfield, NJ). The copper and manganese powders were also obtained from Atlantic Equipment Engineers and were both in the size range of -100 mesh ($\leq 149 \mu\text{m}$, 99.9% purity). The boron powder was obtained in a crystalline form, again from Atlantic Equipment Engineers, in a size range of -100 mesh ($\leq 149 \mu\text{m}$, 93-94% purity). The impurities in the boron were primarily oxides.

Table III: Nominal volume percentage composition of intermetallic matrix composites as estimated from initial chemical analysis.

Designation	A vol % Al_3Ti	B vol % Al_5CuTi_2	C vol % $\text{Al}_{66}\text{Mn}_{11}\text{Ti}_{23}$	Reinforcement vol % TiB_2
IMC 20 A	80			20
IMC 20 B		80		20
IMC 20 C			80	20
IMC 30 A	70			30
IMC 30 B		70		30
IMC 30 C			70	30
IMC 40 A	60			40
IMC 40 B		60		40
IMC 40 C			60	40
IMC 50 A	50			50
IMC 50 B		50		50
IMC 50 C			50	50

The elemental powders for the matrices were prepared in 100 gm batches. The elemental powder formulations for the reinforcement were prepared separately in 200 gm batches.

These powder mixes were homogenized separately on a mixing mill for one hour each.

Table IV shows the nominal weight percentages of the different elemental powders for the different compositions.

Table IV: Weight percentages used to formulate intermetallic matrices and reinforcements for IMCs.

Precursor Material	A Al ₃ Ti	B Al ₅ CuTi ₂	C Al ₆₆ Mn ₁₁ Ti ₂₃	Reinforcement TiB ₂
Aluminum	62.82	45.85	51.07	
Titanium	37.18	32.56	31.6	68.9
Copper		21.59		
Manganese			17.33	
Boron				31.1

In order to form the volume percent of TiB₂ desired the matrix powder was mixed with the Ti/B powder as specified in Table V:

Table V: Weight percentages of matrix and reinforcement materials used to formulate Al₃Ti-based IMCs.

Compound	A Al/Ti Powder	B Al/Ti/Cu Powder	C Al/Ti/Mn Powder	Reinforcement Ti/B Powder
IMC 20 A	74.94			25.06
IMC 20 B		78.13		21.88
IMC 20 C			76.86	23.14
IMC 30 A	63.57			36.43
IMC 30 B		67.57		32.43
IMC 30 C			65.96	34.04
IMC 40 A	52.87			47.13
IMC 40 B		57.25		42.75
IMC 40 C			55.47	44.53
IMC 50 A	42.78			57.22
IMC 50 B		47.17		52.83
IMC 50 C			45.37	54.63

The matrix powder and the Ti/B powder formulations were then mixed in the percentages stated above and homogenized in the mixing mill for one hour. Following blending, the loose powder was cold pressed into cylinders utilizing a hydraulic press at a uniaxial stress of 86.2 MPa (12.5 ksi). The green compacts weighed approximately 20 gm each and were 25.4 mm in diameter x 14 mm high. Reaction synthesis was initiated by induction heating (Power Trak 20-96 power source, VIP Inductotherm Corp., Rancocas, NJ) in a loose graphite foil wrap placed within a graphite crucible. The power was turned up slowly until it reached a set point of 30 kV. The induction heating was conducted under different environments: atmospheric pressure with air, vacuum (~8 Pa), and an inert atmosphere consisting of a partial pressure of argon (3.39×10^4 Pa).

2.3. Comminution of IMC sponge

As-reacted sponge of Al_3Ti , Al_5CuTi_2 , and $\text{Al}_{66}\text{Mn}_{11}\text{Ti}_{23}$ reinforced with 30, 40, and 50 volume % TiB_2 was reduced to fine powder form by jaw crushing and subsequent disk milling. Jaw crushing (Braun LC-34 Chipmunk Jaw Crusher) broke the large sponge into smaller chunks which were subsequently disk milled (Braun LC-67 Lab Pulverizer fitted with LCA-11 Ceramic Pulverizer Plates). This work was conducted at the facilities of Martin-Marietta Laboratories (Baltimore, MD). Sieve analysis on the final powders was performed by mechanical sieve analysis according to ASTM standard B 214-92.³¹

Powders reacted under a partial pressure of argon were mechanically sieved to determine the size of the IMC powder. Figure 4 shows the powder size distribution for the three intermetallic matrices reinforced with 30 volume % TiB_2 . The majority of the weight percent of the powder particles had dimensions between 125 and 300 microns for Al_3Ti matrix composite, and between 75 and 125 microns for the Al_5CuTi_2 and $\text{Al}_{66}\text{Mn}_{11}\text{Ti}_{23}$ matrices. The sieve analysis of the 40 volume percent TiB_2 IMCs showed that the powder size distribution was similar for the 30 volume % reinforced composites; i.e., 125-300 microns for Al_3Ti matrix and 75-125

microns for the Al_5CuTi_2 and $\text{Al}_{66}\text{Mn}_{11}\text{Ti}_{23}$ composites. This is shown graphically in Figure 5.

The sieve analysis of the IMC 50 series showed a different trend. The powder size exhibited relatively even distributions for all size ranges. This is shown in Figure 6.

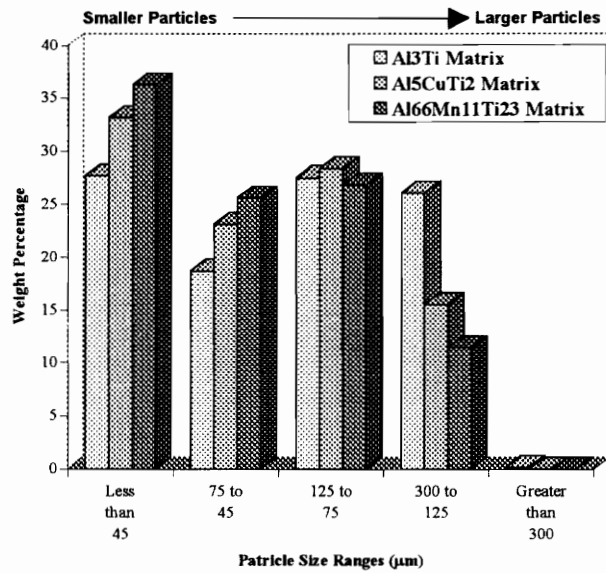


Figure 4: Mechanical sieve analysis of particle size distribution of Al_3Ti , Al_5CuTi_2 , and $\text{Al}_{66}\text{Mn}_{11}\text{Ti}_{23}$ reinforced with 30 volume % TiB_2 .

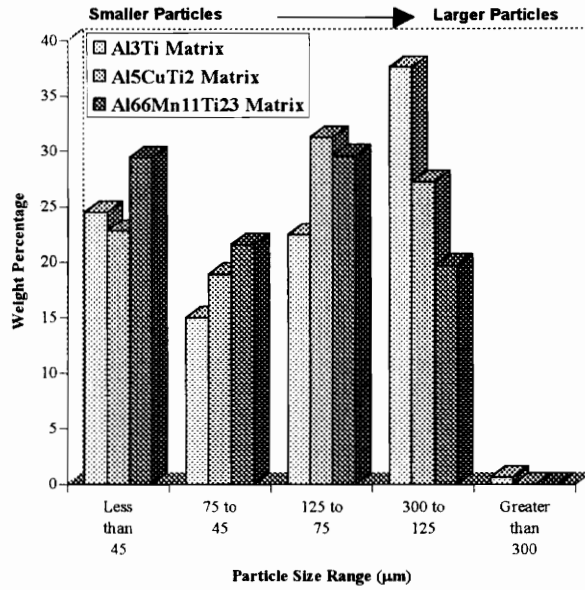


Figure 5: Mechanical sieve analysis of particle size distribution of Al₃Ti, Al₅CuTi₂, and Al₆₆Mn₁₁Ti₂₃ reinforced with 40 volume % TiB₂.

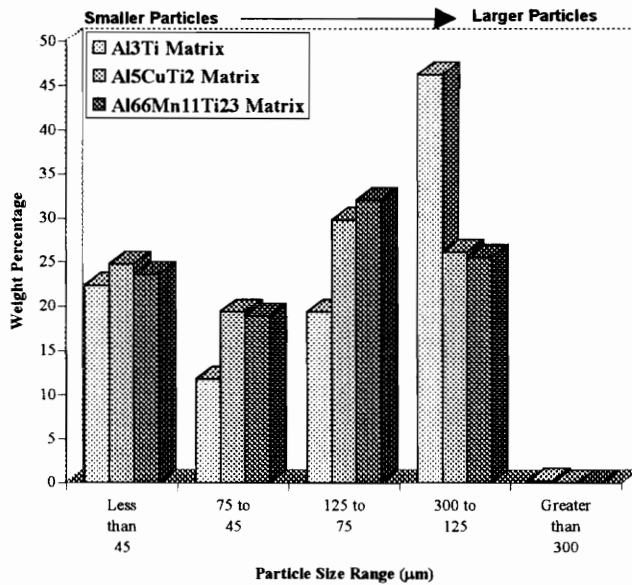


Figure 6: Mechanical sieve analysis of particle size distribution of Al₃Ti, Al₅CuTi₂, and Al₆₆Mn₁₁Ti₂₃ reinforced with 50 volume % TiB₂.

2.4. Consolidation of IMCs

The reacted and size-reduced IMC powders were placed into commercially pure titanium tubes (ASTM grade 2 CP-Ti, 99.86% purity) obtained from President Titanium (Hanson, MA). The tubes had an initial outer diameter of 9.525 mm (3/8 in.) and a wall thickness of 0.9 mm (0.035 in.). The tubes were cut, using an abrasive cutting wheel, to a length of approximately 15.25 cm (6 in.). The tubes were then crimped on one end using a vice and TIG (Tungsten Inert Gas) welded on the crimped end using a Miller Model 250 TIG Metallic Arc Welder (Miller Electric Mfg. Co., Appleton, WI) set to provide straight DC current at 40 amps. These tubes were filled with the IMC powder to a level two inches below the open end of the tube. The tubes were then partially crimped using a tube pinch-off tool (Imperial Eastman 105FF, Chicago, IL) with an opening remaining to allow evacuation. The tubes were placed on a vacuum manifold and evacuated to less than 75 mtorr (9.98 Pa, 75 μ m Hg) over a period of one or more days. During this evacuation process the tubes were heated briefly using an oxyacetylene torch to encourage degassing and drying of the powders. After another 12-24 hours each sample was isolated and completely pinched off at the partially crimped area created before evacuation using the pinch-off tool. The tube was then removed from the manifold, with the pinch-off tool still attached and placed into a waffle crimping die. This die was placed in a hydraulic unidirectional press (Carver model 3437 Lab Press, Menomonee Falls, WI) and the tube was waffle crimped at a pressure of 86.2 MPa (12.5 ksi). The tubes were then

immediately (within 30 minutes) taken to the Physics shop at Virginia Tech sealed using the same TIG welding procedure previously described. Figure 7 shows the evolution of a sample consolidated cylinder.

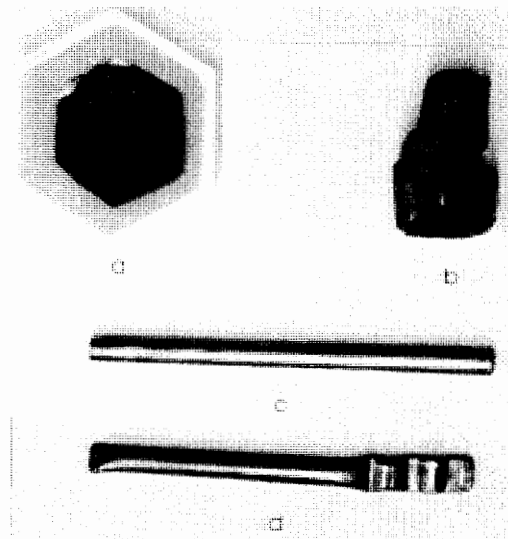


Figure 7: Titanium tubing used in encapsulation of the IMCs. (a) the pre-reacted powder mixture, (b) an as-reacted IMC sponge, (c) titanium tube cut to length, (d) a crimped and welded titanium can. The tube in (c) is 6 inches long.

Each IMC powder-containing tube was pressure tested at approximately 40 MPa (5.8 ksi) for 10 minutes in the chamber of an American Isostatic Press (Pittsburgh, Pa) hot isostatic press (HIP) at the Naval Research Laboratories (Washington, D.C.). The same HIP was then used to consolidate the tubes at a pressure of 205 MPa (30.6 ksi) and a temperature of 1300 °C for a dwell time of 2 hours. Eight samples were placed into the HIP at a time. Following consolidation, the samples were allowed to cool overnight in the chamber of the HIP. A portion of each consolidated cylinder was sectioned and polished

to confirm that the powder had been consolidated. In each case, the powder had consolidated and there was qualitatively no evidence of large pores. A micrograph of a consolidated cylinder section is shown in Figure 8. The most significant feature in this micrograph is the very small pores which appear to be nearly equiaxed.

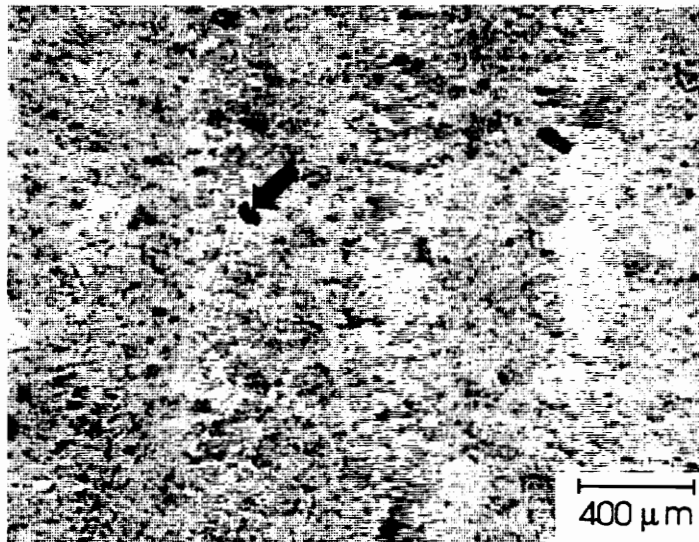


Figure 8: Results of HIP consolidation at 1300°C and 205 MPa for 2 hours. The area indicated by the arrow is the only visible pore with the rest being caused by slight variations within the composite reinforcement distribution. This sample is $\text{Al}_{66}\text{Mn}_{11}\text{Ti}_{23}$ + 40 volume % TiB_2 . (37.5x)

2.5. Compression Testing

Prior to sectioning each sample, the equivalent diameter of the now-consolidated powder "cylinder" within the titanium tubing was measured and recorded. Using this equivalent diameter, the outside of the Ti tubing was marked and sectioned using an abrasive cut-off wheel. The samples were cut to a length such that the aspect ratio was

between 1.5 and 2.0 with respect to the diameter of the consolidated powder cylinder within the tube. The samples were approximately 12-15 mm in height with a round-to-ellipsoidal cross-section of average diameter 6-7.5 mm. The cylinders were ground on the ends using silicon carbide papers to produce flat, parallel surfaces as platen contact points for eventual compression testing. This was checked with the faces of a micrometer. The equivalent diameter was measured using a pair of vernier calipers and recorded. Similarly, a micrometer was used to accurately measure the height. From this information the strain-rates and corresponding crosshead speeds were determined.

The samples were coated in pyrex glass to protect them from oxidation and act as a lubricant at elevated temperatures, thus minimizing the effects of friction on the ends of the samples. This was accomplished by placing a layer of pyrex frit into a small crucible, inserting a sample and then covering the sample with another layer of frit. The crucible was then placed into a box furnace at 1000°C for a period of 30 minutes. The crucible was then removed and allowed to cool to ambient temperature. The excess glass was removed from the sample using a pair of pliers and , in some cases, SiC paper.

The compression testing was performed at the Department of Energy's Oak Ridge National Laboratory in the High Temperature Materials Laboratory User's Center. The samples were tested under compression in an Instron Model 1332 Universal Testing Machine fitted with Series 8500 electronics and a high temperature furnace on rollers which, when in position, surrounded the sample on the compression rams during testing. The compression rams were 19.1mm (3/4in.) diameter rounds of fully densified SiC with

parallel faces to achieve uniform loading. Data acquisition was accommodated using a Daytronics datalogger and an XY chart recorder.

Immediately prior to testing, the glass on the ends of each sample were flattened using emory paper to remove excess glass and facilitate sample loading. This procedure also aided in sample alignment at elevated temperatures. A sample was placed between the silicon carbide platens and a slight pre-load (~300N) was applied to the sample. The furnace was moved into position and heated to testing temperature. Upon achieving test temperature, the sample was allowed to equilibrate for 5 minutes. After 5 minutes the datalogger and chart recorder were started and the sample was compressed at constant crosshead speed in displacement control mode. The sample was allowed to compress until steady-state flow or 15-20% engineering strain was attained, whichever was achieved first.

Following testing, each sample's height was re-measured using a micrometer to determine the plastic strain. This was compared to the amount of plastic strain recorded by the LVDT on the Instron machine and the XY recorder charts. From the variation in these numbers, a correction factor was calculated. The equation for this correction factor is shown below:

$$\epsilon_{corrected} = \epsilon_{computer} \cdot \frac{\epsilon_{measured,final}}{\epsilon_{computer,final}} \quad \text{Equation 2-1}$$

The values from the Daytronics appeared more consistent in their variation and so they were corrected and used to represent the flow behavior of the material.

Data for each test was compiled and plotted as stress versus strain using the corrected strain. Further details of this analysis are provided in Chapters 3 and 4.

2.6. Metallographic Preparation

Metallographic analysis was performed on both the as-reacted sponge and the as-HIP'd cylinders. In both cases specimens were mounted in bakelite resin. The as-reacted samples were ground on SiC papers and further polished with alumina powders or colloidal silica on billiard cloth and brushed twill. This polishing was performed on a Leco VP-50 polishing wheel equipped with an AP-50 semi-automatic polishing head and load controller. The as-HIP'd samples were rough-polished using a series of diamond compounds from 9 to 0.1 microns on a Buehler Ecomet 3 polishing wheel covered by nylon cloth and attached to an Automet 2 polishing head with a Metlap 2000 polishing fluid dispenser.

All samples were examined as polished and as etched by a 2 vol % HF solution in water. The microscopic observations were made on an Olympus BH2-UMA microscope using Nomarski differential interference contrast and polarized light. Environmental scanning electron microscopy (ESEM) was performed on several samples using an Electroscan model E3 microscope. The ESEM contained an electroscan energy dispersive x-ray analyzer (EDAX) allowing a qualitative analysis of the reinforcing phase of the composites.

2.6.1. TiB₂ crystal size analysis

The size of the TiB₂ crystals were measured from high magnification (~1500x) micrographs using a hand held magnifying (7x) eyepiece to measure the major diameter and the diameter perpendicular to it. To limit the degree of measuring prejudice, a random 1.5 inch square of clear micrograph was sectioned from the rest of the photo by using a cardboard "window". After eliminating any particles which were not completely within the 1.5 inch window, every visible particle was measured. The equivalent diameter was calculated based on the diameter of a sphere of area equivalent diameter to the ellipsoidal area calculated from the aforementioned measurements. The aspect ratio ($d_{\text{major}}/d_{\text{perpendicular}}$) of the particles was also calculated.³²

2.6.2. TiB₂ crystal spacing analysis

The interparticle spacing of the TiB₂ crystals was measured using the line intercept method to measure the center-to-center particle spacing, $\lambda_{\text{c-c}}$. A statistical correction was used to adjust the equivalent diameter in the second term to correct for non-diametrical measurements. The equation used to calculate the edge-to-edge spacing (including a correction factor of 0.816 which accounts for non-planimetric particle diameters)³² is shown below:

$$\lambda_{\text{e-e}} = \lambda_{\text{c-c}} - 0.816 \cdot \bar{d}_{\text{measured}} \quad \text{Equation 2-2}$$

This measured and calculated value was compared to a purely calculated value using the equation below:³²

$$\lambda_{e-e} = 1.225 \cdot \bar{r}_{\text{measured}} \left(\frac{2\pi}{3f} \right)^{\frac{1}{2}} - 1.63 \cdot \bar{r}_{\text{measured}} \quad \text{Equation 2-3}$$

where f is the volume fraction of reinforcement. In this way the nominal volume fraction of TiB_2 could be compared to the calculated values.

2.6.3 X-ray Diffraction Analysis

X-ray diffraction analysis was performed on several samples to confirm the presence of the expected phases and identify contaminants. Samples from the actual compression testing were polished on one side to reveal a rectangular cross-section of the right cylindrical test specimen. The samples were tested in the Scintag DCM 2000 at Virginia Tech's Materials Characterization Center. The polished and flattened cross-section was exposed to x-ray radiation and diffraction peak patterns were generated. Further information on this analysis is available in chapters 3 and 4.

3. EXPERIMENTAL RESULTS

3.1. Reaction Synthesis

3.1.1. Formulation and Conditions

In the reaction synthesis of the IMCs, three variables were investigated in an attempt to produce IMCs with a wide range of high temperature flow properties. First, the reaction synthesis was performed for four volume percentages of TiB₂ within the intermetallic solvent: 20, 30, 40 and 50 volume %. The second variable was the intermetallic matrix itself. Three matrices were investigated: Al₃Ti, Al₅CuTi₂, and Al₆₆Mn₁₁Ti₂₃. The copper and manganese modified aluminides were chosen because they possess melting temperatures lower than that of the Al₃Ti system.²²⁻²⁴ This depressed melting temperature might be reflected in lower flow stresses at test temperature. The third variable investigated was the use of different atmospheres within the reaction chamber. Processing atmosphere has been shown to influence the size and shape of the ceramic reinforcement as well as the presence of contaminants within the IMC sponge.²⁸ Three atmospheres were studied: air at atmospheric pressure, low vacuum (evacuated to 7.98 Pa) and a partial pressure of argon (evacuated to 7.98 Pa and then restored to

2.93kPa with argon.) Table VI summarizes these conditions with the sample designations for each.

Table VI: Different Conditions Used for the synthesis of Al₃Ti-based IMCs and their designations.

Al₃Ti Matrix	20 vol.% TiB₂	30 vol.% TiB₂	40 vol.% TiB₂	50 vol.% TiB₂
Air	IMC 20 A1	IMC 30 A1	IMC 40 A1	IMC 50 A1
Vacuum	IMC 20 A2	IMC 30 A2	IMC 40 A2	IMC 50 A2
Partial Argon	IMC 20 A3	IMC 30 A3	IMC 40 A3	IMC 50 A3
Al₅CuTi₂ Matrix	20 vol.% TiB₂	30 vol.% TiB₂	40 vol.% TiB₂	50 vol.% TiB₂
Air	IMC 20 A1	IMC 30 A1	IMC 40 A1	IMC 50 A1
Vacuum	IMC 20 A2	IMC 30 A2	IMC 40 A2	IMC 50 A2
Partial Argon	IMC 20 A3	IMC 30 A3	IMC 40 A3	IMC 50 A3
Al₆₆Mn₁₁Ti₂₃ Matrix	20 vol.% TiB₂	30 vol.% TiB₂	40 vol.% TiB₂	50 vol.% TiB₂
Air	IMC 20 A1	IMC 30 A1	IMC 40 A1	IMC 50 A1
Vacuum	IMC 20 A2	IMC 30 A2	IMC 40 A2	IMC 50 A2
Partial Argon	IMC 20 A3	IMC 30 A3	IMC 40 A3	IMC 50 A3

3.1.2. Qualitative Description of the Reaction Synthesis

The brightness of the reacting pellets, which can be seen through an upper window in the environmental chamber during the reaction synthesis, gives a qualitative means to compare the temperature of the reaction with respect to the TiB₂ content. The velocity of the reaction can be gauged in the same way. The graphite crucible placed within the induction coil, requires about 90 seconds to reach a temperature hot enough to initiate the

reaction. As the reaction occurs, the faint orange glow of the heated pellet rapidly becomes white hot and occasionally splatters around the inside of the chamber.

3.1.2.1. Effect of volume % TiB_2 on the reaction

As the pellets begin to heat they become bright orange and emit white vapors, believed to be volatile oxides from the powder mixes or volatilization of the aluminum powder. When the pellet reaches the initiation temperature for the reaction, believed to be between $600^\circ\text{-}1000^\circ\text{C}$, the induction source is turned off and the exothermic reaction consumes the pellet in a bright white glow. This reacted pellet subsequently ignites the remaining pellets within the crucible. In every case the reaction lasts less than 5 seconds. The actual duration and intensity of the reaction varies with the volume percentage of TiB_2 within the Al_3Ti -based solvent.

The amount of heating and the intensity of the reaction are both a function of the volume percent of TiB_2 . Lower volume percent TiB_2 , as in IMC 20 and IMC 30, require about 1 minute of heating before the reaction actually begins. As the percentage of TiB_2 increases the heating time also increases to about 2 minutes of heating for IMC 50. This increased heating time is due to the decreased amount of molten aluminum. Because the self-sustenance of the reaction is driven by the exothermic formation of TiB_2 , the decrease in molten aluminum makes the titanium and boron combination less accessible. The intensity of the reaction, qualitatively a measure of its temperature, also increases with increasing volume percent TiB_2 . IMC 50 pellets glow bright white and emit a good deal

of vapor as the reaction occurs. IMC 20 reactions exhibit less brightness and are less likely to splatter molten aluminum around the reaction chamber.

3.1.2.2. Effect of the matrix composition on the reaction

The matrix composition did not appear to greatly affect the reaction synthesis. In both modified matrices the alloying elements are known to substitute primarily into the aluminum sites, leaving slightly less aluminum than in the Al_3Ti -matrices for use as a solvent in the reaction.³³ Again, however, clouds of white vapor occurred prior to reaction. This indicates that some aluminum may be volatilizing. Although not confirmed via x-ray diffraction or chemical analysis techniques, the aluminum volatilization is evidenced by the formation of a white/gray film which forms on the inside of the upper observation window in the reaction chamber after several subsequent reactions.

3.1.2.3. Effect of the atmosphere on the reaction

Reactions occurring in air have a small amount of white or light gray oxide on the outer shell of the reacted pellets. These are believed to be titanium and/or aluminum oxides.

The low vacuum made for reactions in which much of the IMC was lost due to the splatter mentioned in 3.1.2. Pre-reaction degassing occurred readily, as evidenced by the loss of complete vacuum and the appearance of clouds of smoke-like vapors. As the IMC

reacted, a volcano of molten material could be seen within the graphite crucible, especially at higher volume percentages of TiB_2 . This splattering was also evidenced by the many small beads and granules of materials strewn about the inside of the reaction chamber. The reacted products from this environment were very porous and dull grey in color. None of the aforementioned white oxides were present. The vacuum reacted pellets were very difficult to extract from their graphite wraps as the pellets seemed to have melted into the wraps in many cases.

Pellets reacted in a partial pressure of argon (3.39×10^4 Pa) did not react violently, as they had in the vacuum. The presence of pre-reaction vapors was observed, but not in the abundance of those in the vacuum reactions. The reacted pellets looked like shiny mushrooms with large amounts of internal porosity. The size of these internal pores varied greatly, but did not follow any trend with respect to matrix composition or volume percentage reinforcement. The reacted pellets were dull gray where they were in contact with graphite foil wraps, shiny and metallic elsewhere. It is believed that this is evidence of carbide formation during the reaction synthesis.

3.2. Microstructural Analysis

3.2.1. Matrix Microstructures

The microstructural features of the matrix were investigated using optical microscopy and x-ray diffraction. These features include a multiphase matrix and the appearance of a basketweave structure in the Al_5CuTi_2 -matrix composites.

3.2.1.1. Effects of Matrix Composition on Microstructure

Optical microscopy revealed similar microstructures in all three matrices. In every case, the presence of TiB_2 is evident throughout the structure as a uniform distribution of faceted prism-shaped crystal prisms. The matrix composition had little or no effect on the aspect ratio of the TiB_2 . The effect of the matrix composition on the particle size and interparticle spacing did not follow any discernable trend. A typical microstructure is shown in Figure 9.

Deviation from the typical microstructures did occur in a few cases. Of particular interest is the basketweave pattern present in the $\text{Al}_5\text{CuTi}_2 + 30$ volume % TiB_2 and $\text{Al}_5\text{CuTi}_2 + 40$ volume % TiB_2 samples. Although not observed in the $\text{Al}_5\text{CuTi}_2 + 50$ volume % TiB_2 , it is suspected that the same basketweave pattern is present but masked by the high loading of TiB_2 in this sample. This microstructure is shown in Figure 10. This type of microstructure occurs in samples both before and after HIP'ing at 1300°C and

205 MPa for 2 hours. In addition, there are regions in the Al_5CuTi_2 -matrix samples which appear to have more than one matrix phase. This is shown as different shaded regions in Figures 11 and 12. This second micrograph also shows large regions where TiB_2 crystals have been fused together during the reaction synthesis. At lower magnification the basketweave structure remains visible in $\text{Al}_5\text{CuTi}_2 + 30$ volume % TiB_2 . In any case, the presence of multiphase regions in the Al_3Ti and Al_5CuTi_2 matrix composites is most likely a mixture of the Al_3Ti or Al_5CuTi_2 and TiAl phases. This would be the result of an aluminum lean composition. This multiphase composition was also verified by means of x-ray diffraction analyses.

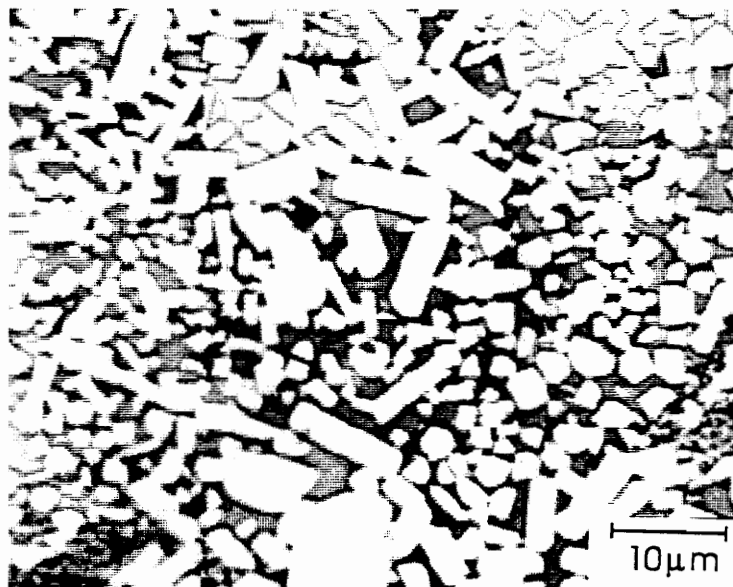


Figure 9: A typical micrograph of the as-polished intermetallic matrix composites. Note the presence of TiB_2 crystals throughout. This particular sample is $\text{Al}_5\text{CuTi}_2 + 40$ vol% TiB_2 .

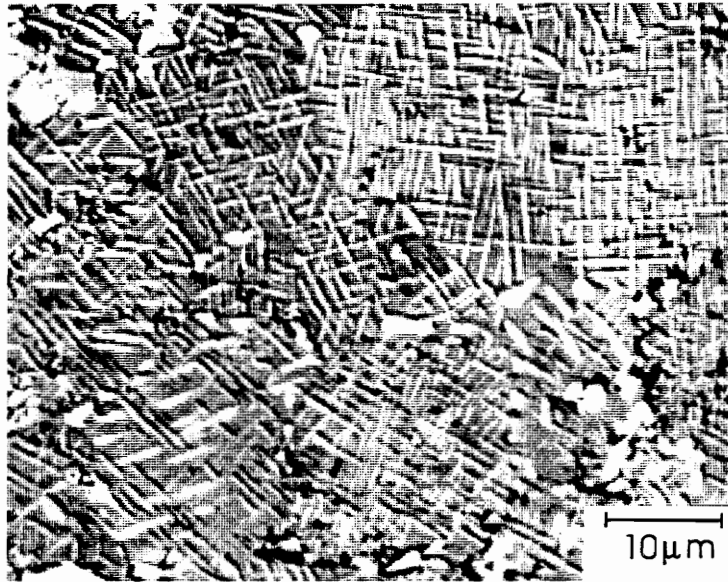


Figure 10: Micrograph of the basketweave structure observed in Al_3CuTi_2 + 30 and 40 volume % TiB_2 after HIP'ing at 1300°C and 205 MPa for 2 hours.

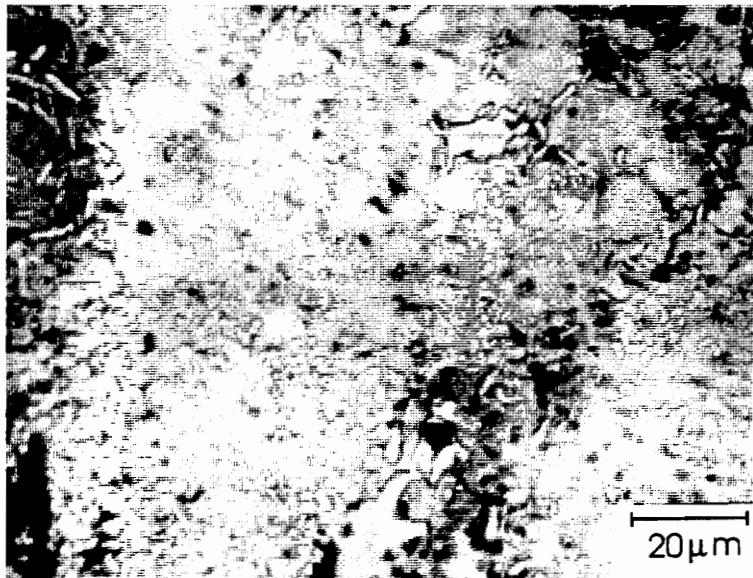


Figure 11: Multiphase regions appear as different shades of gray in the matrix portion of the composite in a sample of Al_3Ti + 30 volume % TiB_2 .



Figure 12: Multiphase regions appear as different shades of gray in the matrix portion of the composite in a sample of Al_3CuTi_2 + 30 volume % TiB_2 .

3.2.1.2. X-ray Diffraction Analysis of As-tested Samples

3.2.1.2.1. XRD of Al_3Ti matrix composites

X-ray diffraction of samples of selected Al_3Ti reinforced with 30, 40, and 50 volume % TiB_2 all revealed similar diffraction patterns. In all cases the presence of TiB_2 , Al_3Ti , and TiAl was detected. A typical diffraction peak diagram is shown in Figure 13. The presence of TiAl in the matrix of the composite indicates that the composites were formed on the aluminum lean side of the Al_3Ti composition line. In the future this off-composition problem could be addressed by the addition of extra aluminum powder in

the green compacts prior to reaction synthesis. However, due to the increasing temperature of reaction with increasing volume % TiB_2 , it is unlikely that this extra amount of aluminum would be constant for all volume % reinforcements.

3.2.1.2.2. XRD of Al_3CuTi_2 matrix composites

The results of the x-ray analysis of the Al_3CuTi_2 matrix samples were very similar to those of the Al_3Ti -based samples. As expected, TiB_2 appeared as the most discernable peaks. The presence of Al_3CuTi_2 was also observed. Figure 14 shows a typical x-ray diffraction pattern for the Al_3CuTi_2 -matrix samples.

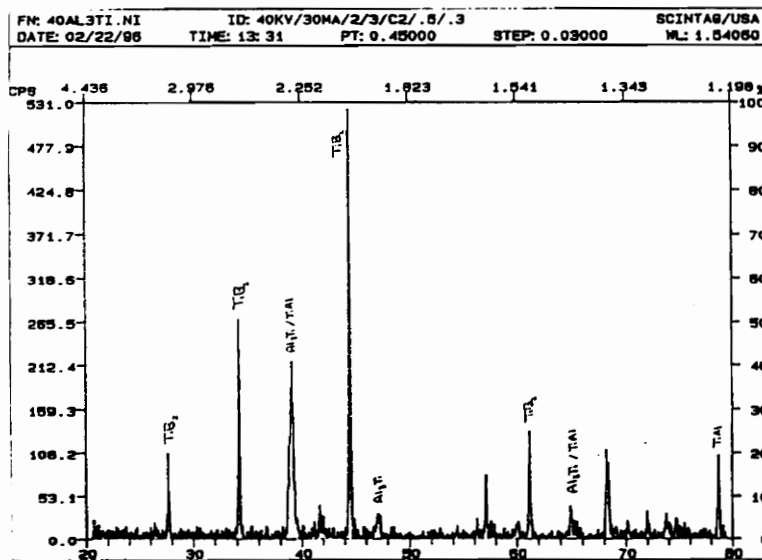


Figure 13: An X-ray Diffraction peak pattern from Al_3Ti + 40 volume % TiB_2 . This pattern is typical of all of the Al_3Ti matrix compositions.

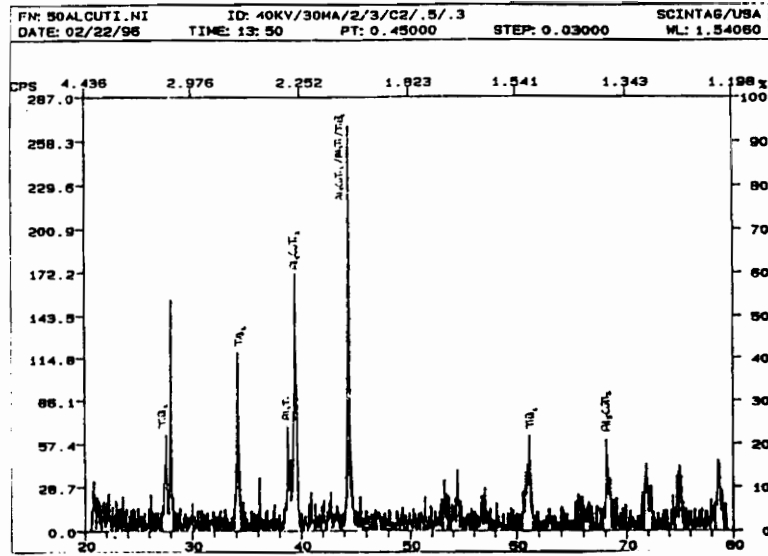


Figure 14: An x-ray diffraction pattern from $\text{Al}_3\text{CuTi}_2 + 40$ volume % TiB_2 . This pattern is typical of the Al_3CuTi_2 -matrix composites.

3.2.2. Analysis of Dispersed TiB_2 Particulates

The presence of the TiB_2 single crystals is evident in the microstructure of all the IMCs. These crystals have a faceted appearance and are between $0.1 \mu\text{m}$ and $20 \mu\text{m}$ in diameter at the extremes. The average TiB_2 particle sizes, with 95% confidence intervals, are shown in Table VII. The average particle size measurements were repeated until a relative accuracy below 15% was achieved. The trends in the average particle size of the TiB_2 reinforcements is shown in Figure 15. Both the Al_3Ti - and Al_3CuTi_2 -matrix composites exhibited maximum TiB_2 particle size in the samples reinforced with 40 volume % TiB_2 . The $\text{Al}_{66}\text{Mn}_{11}\text{Ti}_{23}$ -matrix composites showed the opposite trend, with the smallest particle size occurring in the 40 volume % reinforced configuration.

The average equivalent diameter of a TiB_2 crystal for all composites was $2.17 \pm 0.20 \mu\text{m}$. The aspect ratios of these particulates was also measured and found to be relatively constant. The average aspect ratio is 1.55 ± 0.11 for all IMCs. The actual values of the aspect ratios are shown in Figure 16.

The interparticle spacing was also calculated for the composites. In every case the Al_5CuTi_2 -matrix composites exhibited the widest particle spacing. The Al_3Ti - and $\text{Al}_{66}\text{Mn}_{11}\text{Ti}_{23}$ -matrix composites clearly show that as the volume % of reinforcement increases, the interparticle spacing decreases. This trend line has also been applied to the Al_5CuTi_2 -matrix composites, though the relationship is not as distinct. These lines and the measured values for the interparticle spacings are shown in Figure 17. The average interparticle spacing was determined to be $0.94 \mu\text{m}$ for the Al_3Ti -matrix composites, $3.01 \mu\text{m}$ for the Al_5CuTi_2 -matrix composites, and $0.81 \mu\text{m}$ for the $\text{Al}_{66}\text{Mn}_{11}\text{Ti}_{23}$ -matrix composites. The spacing was also calculated using Equation 2-3 which incorporates the measured equivalent diameter and the nominal volume fraction of reinforcement. These results are compared to the as-measured values in Table VIII.

Table VII: TiB₂ average particle size and 95% confidence intervals from manual measurements.

Composite	Average Particle Diameter (μm)	95% Confidence Interval (μm)	Composite	Average Particle Diameter (μm)	95% Confidence Interval (μm)
IMC 20 A1	1.3	±0.23	IMC 40 A1	2.2	±1.3
IMC 20 A2	6	±2.07	IMC 40 A2	1.7	±0.31
IMC 20 A3	2.3	±1.06	IMC 40 A3	3	±0.26
IMC 20 B1	2.4	±0.85	IMC 40 B1	1.4	±0.35
IMC 20 B2	1.5	±0.27	IMC 40 B2	1.7	±0.31
IMC 20 B3	3	±0.96	IMC 40 B3	2.8	±0.23
IMC 20 C1	1.3	±0.26	IMC 40 C1	1.3	±0.17
IMC 20 C2	2.7	±1.06	IMC 40 C2	1.7	±0.75
IMC 20 C3	1.8	±0.44	IMC 40 C3	1.8	±0.13
IMC 30 A1	1.5	±0.29	IMC 50 A1	1.2	±0.17
IMC 30 A2	*	*	IMC 50 A2	2.2	±0.76
IMC 30 A3	1.8	±0.19	IMC 50 A3	2.6	±0.24
IMC 30 B1	1.4	±0.35	IMC 50 B1	1.5	±0.22
IMC 30 B2	*	*	IMC 50 B2	2.5	±0.9
IMC 30 B3	2.3	±0.35	IMC 50 B3	0.8	±0.12
IMC 30 C1	1.4	±0.17	IMC 50 C1	1.4	±0.19
IMC 30 C2	2.4	±0.83	IMC 50 C2	1.4	±0.44
IMC 30 C3	2.1	±0.14	IMC 50 C3	2.2	±0.24

*Particles were below manual measurement resolution.

1. "A" designations refer to the binary Al₃Ti matrix, "B" designations refer to the ternary Al₅CuTi₂ matrix, and "C" designations refer to the ternary Al₆₆Mn₁₁Ti₂₃ matrix
2. "1" designations refer to compositions reacted in air, "2" designations refer to compositions reacted under vacuum, and "3" designations refer to compositions reacted under a partial pressure of argon.

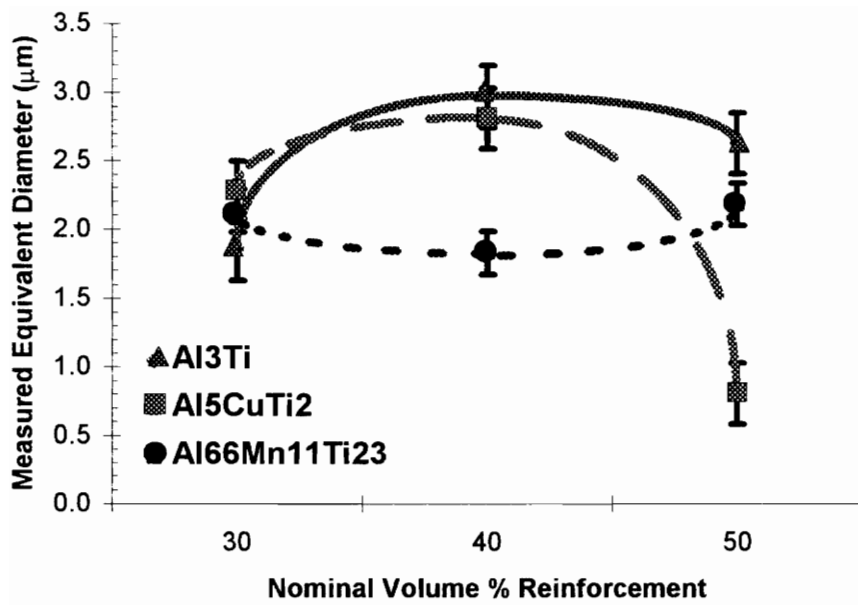


Figure 15: Average particle size of TiB₂ reinforcements in the as-reacted intermetallic matrix composites reacted under a partial pressure of argon.

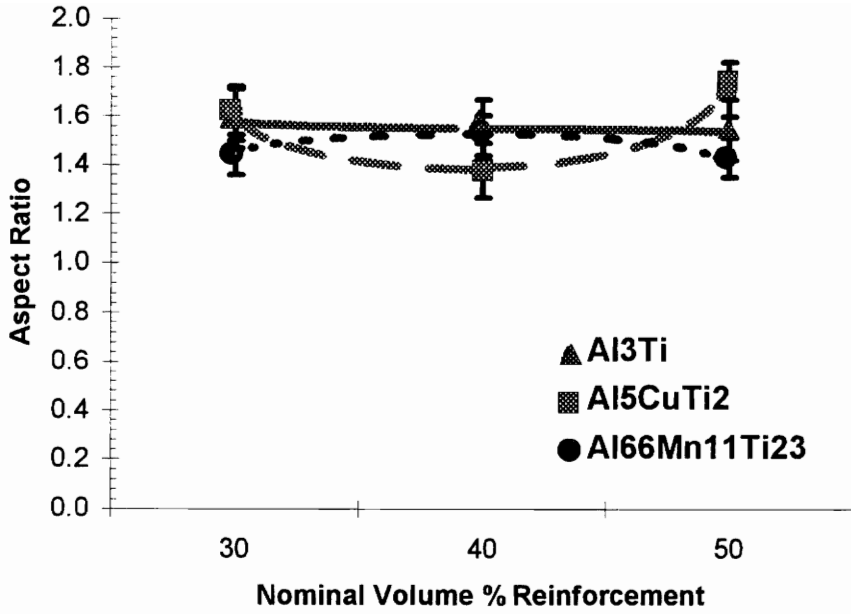


Figure 16: Average aspect ratio of TiB_2 particulate reinforcements in the as-reacted intermetallic matrix composites reacted under a partial pressure of argon.

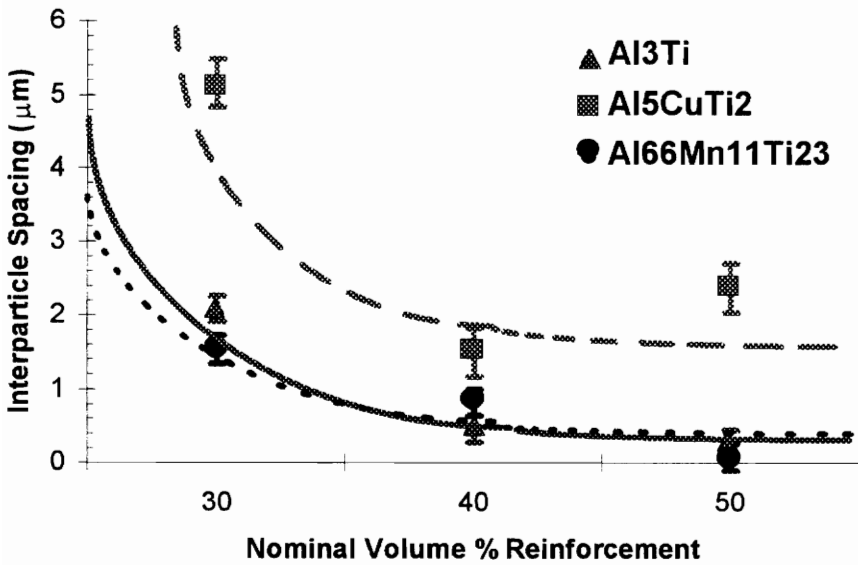


Figure 17: Average interparticle spacing of the TiB_2 reinforcements in the as-HIP'd intermetallic matrix composites originally reacted under a partial pressure of argon. The interparticle spacing is roughly proportional to $(\text{volume fraction})^{-1/3}$.

Table VIII: A comparison of the measured interparticle spacing and the as-calculated interparticle spacing.

Sample Designation ¹	Spacing ² _{measured} (μm)	Spacing ³ _{calculated} (μm)
IMC 30 A	2.09 ± 0.24	1.52
IMC 30 B	5.17 ± 0.43	1.85
IMC 30 C	1.54 ± 0.27	1.68
IMC 40 A	0.46 ± 0.17	1.76
IMC 40 B	1.5 ± 0.31	1.64
IMC 40 C	0.82 ± 0.16	1.05
IMC 50 A	0.27 ± 0.13	1.14
IMC 50 B	2.37 ± 0.26	0.35
IMC 50 C	0.08 ± 0.13	0.96

1. Example of sample designation: IMC 30 A = Al₃Ti ("A" matrix) + 30 volume % TiB₂.

2. Using equation 2-2:

$$\lambda_{e-e,measured} = \lambda_{c-c,measured} - 1.63 \cdot \bar{r}_{measured}$$

3. Using equation 2-3:

$$\lambda_{e-e,measured} = 1.225 \cdot \bar{r}_{measured} \sqrt{\frac{2\pi}{3f}} - 1.63\bar{r}_{measured}$$

3.3. Mechanical Behavior

3.3.1. General

A typical stress-strain curve for the TiB₂-reinforced intermetallic composites is shown in Figure 18. A list of the compression tests performed and the corresponding peak flow stresses is shown in Table IX. The results of five of these tests are believed to be erroneous due to an equipment failure which was not recognized at the time. These suspected errors are highlighted in Table IX and are not used in later calculations except

where noted. These points are also circled whenever they appear within a plot and the corresponding trendline is indicated by a broken line.

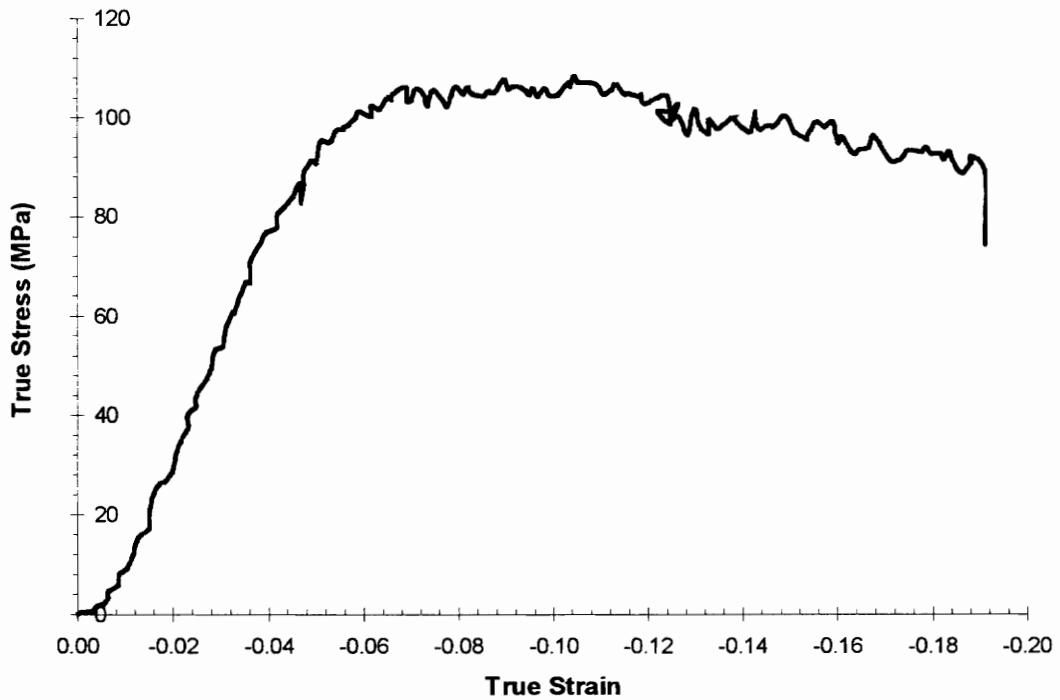


Figure 18: A typical true stress vs. true strain curve. This particular curve is from a compression test of $\text{Al}_3\text{Ti} + 30$ volume % TiB_2 at 1100°C and 0.001 sec^{-1} .

Table IX: The true plastic stress peaks and the true plastic strains at which those peaks occur (after application of a correction factor).

Sample and Test Designation	Peak True Plastic Stress (MPa)	Sample and Test Designation	Peak True Plastic Stress (MPa)	Sample and Test Designation	Peak True Plastic Stress (MPa)
30A 1000/.0001	150	40A 1000/.0001	45	50A 1000/.0001	114
30A 1100/.0001	23	40A 1100/.0001	16.5	50A 1100/.0001	34
30A 1200/.0001	3.8	40A 1200/.0001	11.2	50A 1200/.0001	8
30A 1000/.001	145	40A 1000/.001	62	50A 1000/.001	1,025
30A 1100/.001	105	40A 1100/.001	36	50A 1100/.001	79
30A 1200/.001	66	40A 1200/.001	15.7	50B 1000/.0001	240
30B 1000/.0001	133	40B 1000/.0001	230	50B 1100/.0001	79
30B 1100/.0001	53	40B 1100/.0001	82	50B 1200/.0001	13
30B 1000/.001	220	40B 1100/.0005	141	50B 1100/.0005	105
30B 1100/.001	25	40B 1000/.001	335	50B 1000/.001	318
		40B 1100/.001	123	50B 1100/.001	97
				50B 1200/.001	34

3.3.2. Development of Constitutive Equations

The phenomenologically-based constitutive equations to be developed are based upon the flow stress equation:³⁴

$$\sigma_{flow} = A \cdot \dot{\epsilon}^m \exp \left[\frac{mQ}{RT} \right] \quad (\text{Equation 3-1})$$

Use of this equation requires the determination of the strain rate exponent (m), the activation energy required for deformation (Q), and the structure constant (A). In this

work, the constitutive equation will be developed for values of flow stress corresponding to the peak true plastic stress. The strain-rate sensitivity and the activation energy may be derived by isolating each using the partial derivative of the flow stress equation with respect to the strain-rate or the inverse of the temperature, respectively.

3.3.2.1. The Strain-rate Sensitivity, m

Strain-rate sensitivity plots are generated for each of the three test temperatures by plotting the true plastic stress peaks versus the strain-rate on a log-log scale. A trend line is drawn by using the points for each IMC composition. This line has a slope equal to the strain-rate sensitivity. The equation for this slope is:

$$m = \left(\frac{\partial \ln \sigma}{\partial \ln \dot{\epsilon}} \right)_T \quad (\text{Equation 3-2})$$

Figures 19, 20, and 21 show these relationships for temperatures of 1000°, 1100°, and 1200°C, respectively. Table X is a compilation of the strain-rate sensitivity values for each composite at each test temperature. The average strain-rate sensitivity for all temperatures was found to be 0.349 for the Al_3Ti -matrix composites, and 0.247 for the Al_5CuTi_2 -matrix composites.

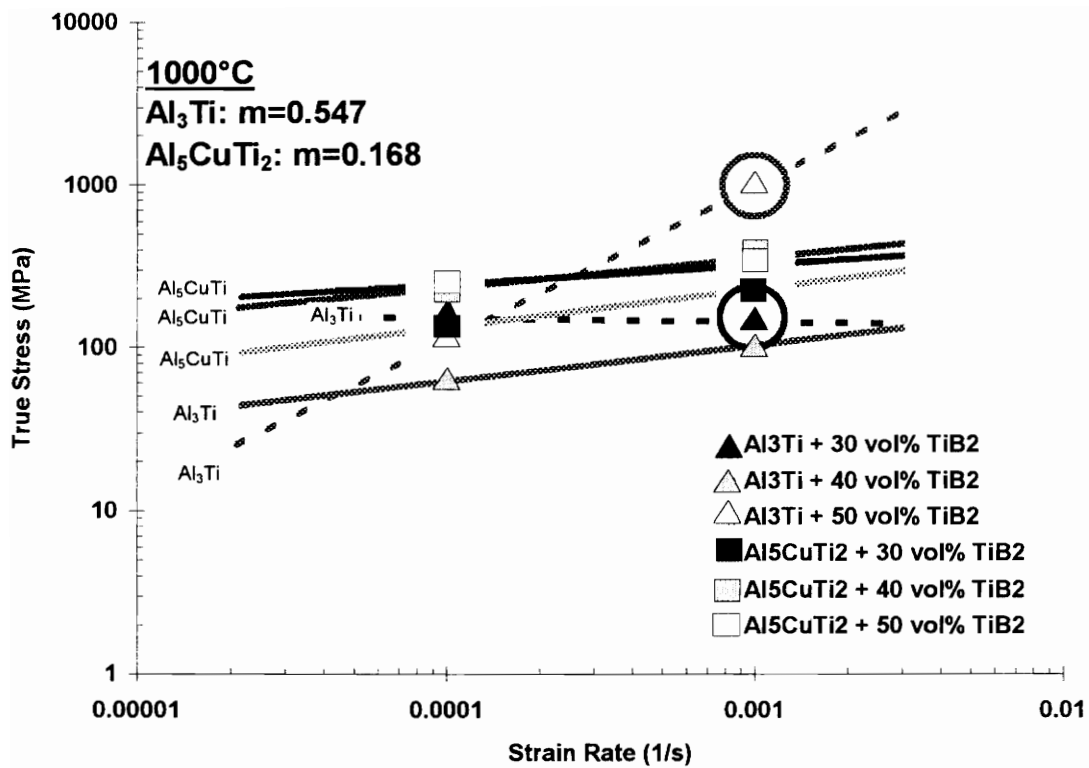


Figure 19: Plot of true peak stress versus strain rate for each composite at 1000°C. The slope of the trace of a line drawn between the points for each composite is equal to that composite's strain rate sensitivity, m . Circled points were not used in the actual calculation of the strain-rate sensitivity. Dashed lines represent questionable strain-rate sensitivity values and are not reflected in average m values.

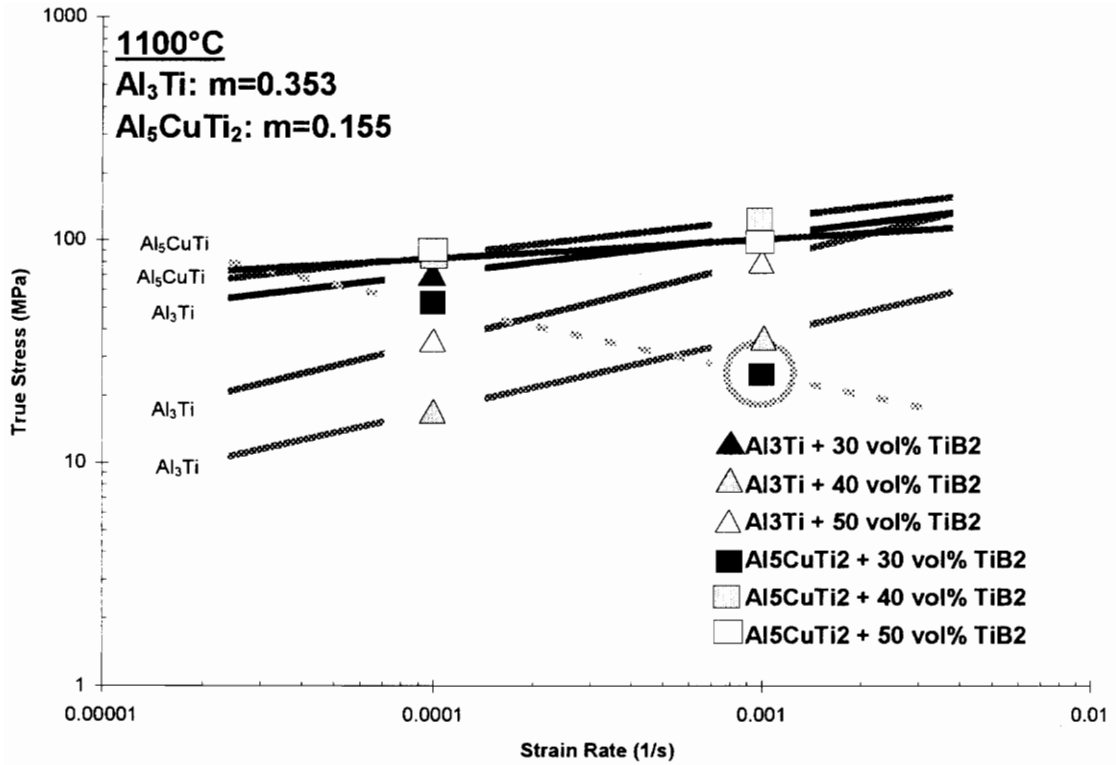


Figure 20: Plot of true peak stress versus strain rate for each composite at 1100°C. The slope of the trace of a line drawn between the points for each composite is equal to that composite's strain rate sensitivity, m . Circled points were not used in the actual calculation of the strain-rate sensitivity. The dashed line represents a questionable strain-rate sensitivity value and are not reflected in average m values.

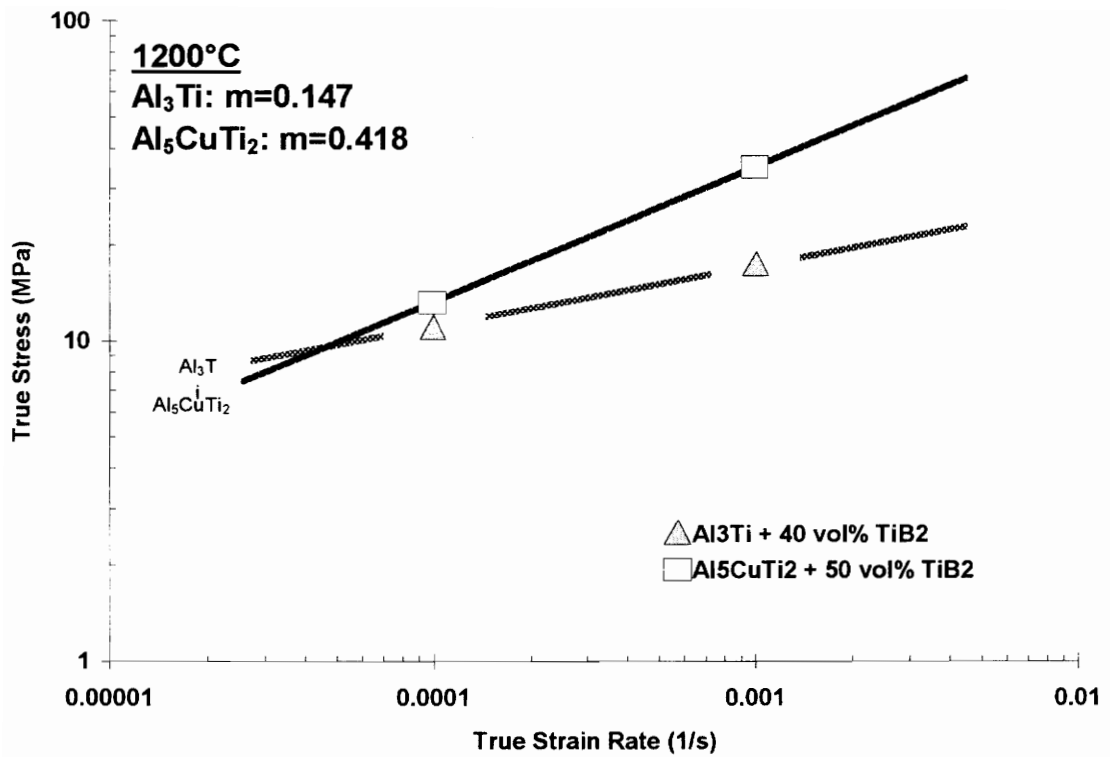


Figure 21: Plot of true peak stress versus strain rate for each composite at 1200°C. The slope of the trace of a line drawn between the points for each composite is equal to that composite's strain rate sensitivity, m .

Table X: Strain-rate sensitivity values for each composite at each test temperature.

Composite Designation ¹	1000°C	1100°C	1200°C	Average over all temperatures
IMC 30A ²	-0.015 ³	0.659 ³		
IMC 40A	0.139	0.339	0.147	0.208
IMC 50A	0.954	0.366		0.66
Average for Al ₃ Ti's	0.547	0.353	0.147	0.349
IMC 30B	0.219	-0.326 ³		0.219
IMC 40B	0.163	0.204		0.184
IMC 50B	0.122	0.105	0.418	0.215
Average for Al ₅ CuTi ₂ 's	0.168	0.155	0.418	0.247
Average for all composites	0.358	0.254	0.283	0.298

1. Example of composite designation: IMC 30A = Al₃Ti ("A" matrix) + 30 volume % TiB₂.
2. Tests conducted at 1000°C and 1100°C contain erroneous data.
3. This value was not used to calculate averages.

Table XI summarizes the results of the strain-rate sensitivity calculations. Three inconsistencies were observed in these calculations. Two occurred in the Al₃Ti + 30 volume % TiB₂ tests at 1000° and 1100°C. The other inconsistent value was determined for Al₅CuTi₂ + 30 volume % TiB₂ tested at 1100°C. These three values are believed to be due to the temperature measurement error as discussed in section 3.3.1 and have not been used in the calculation of the average strain-rate sensitivity values found in Table XI.

3.3.2.2. The Activation Energy, Q

The activation energy is determined in a manner similar to the strain-rate sensitivity. In this case, a linear relationship is obtained when the log of the strain rate is plotted as a function of inverse temperature. A trend line is generated using the points for

each of the IMC compositions. The slope of this trend line is related to the activation energy as shown in the equation below:

$$\frac{mQ}{R} = \left(\frac{\partial \ln \sigma}{\partial \frac{1}{T}} \right)_{\dot{\epsilon}} \quad \text{Equation 3-3}$$

The value for the activation energy, Q , is dependent on the calculated value for the strain-rate sensitivity. Any inconsistencies in the strain-rate sensitivity value, will, therefore, be reflected in the value determined for the activation energy. The actual calculated strain-rate sensitivity values were used whenever possible, however in the inconsistent cases noted previously, the average values of the strain-rate sensitivity for each composite matrix were used.

Figures 22 and 23 show the linear relationships used to determine the activation energies. Table XI shows the activation energy values calculated from the Figures 22 and 23. The average activation energies for the composites was determined to be 485 kJ/mol for the Al_3Ti -matrices and 920 kJ/mol for the Al_5CuTi_2 -matrices. The circled points in Figures 26 represent the results which were not used in the calculation of the activation energy because of the temperature measurement errors mentioned previously.

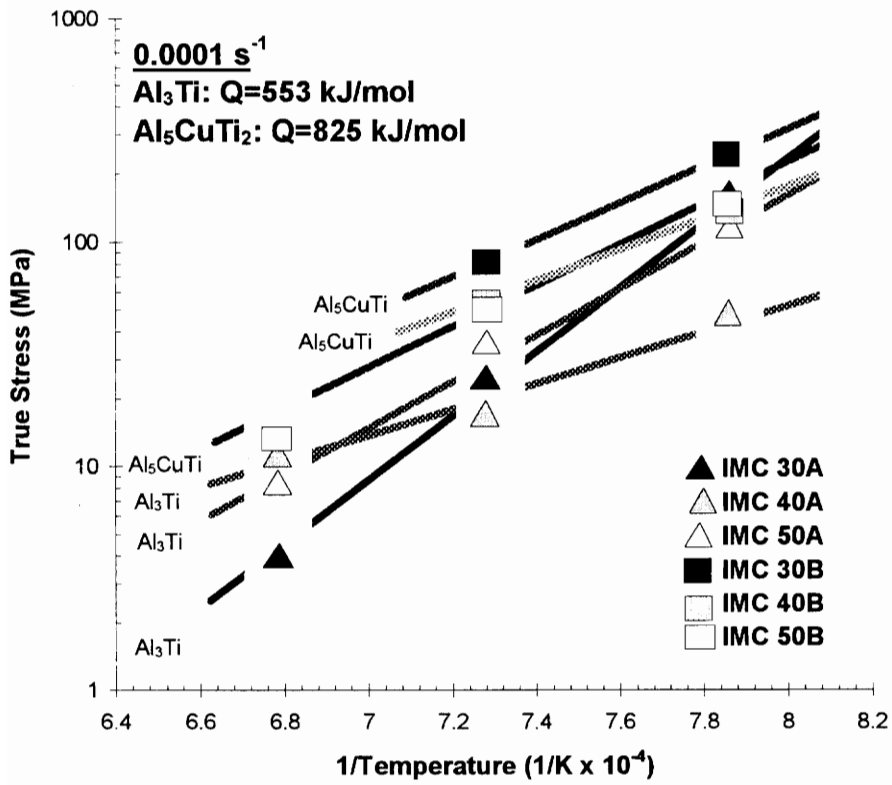


Figure 22: Plot of the true peak stress versus the inverse temperature on a log-linear scale for each of the composites at 0.0001 s^{-1} . The slope of the trace of a trend line for each composition is that composite's activation energy.

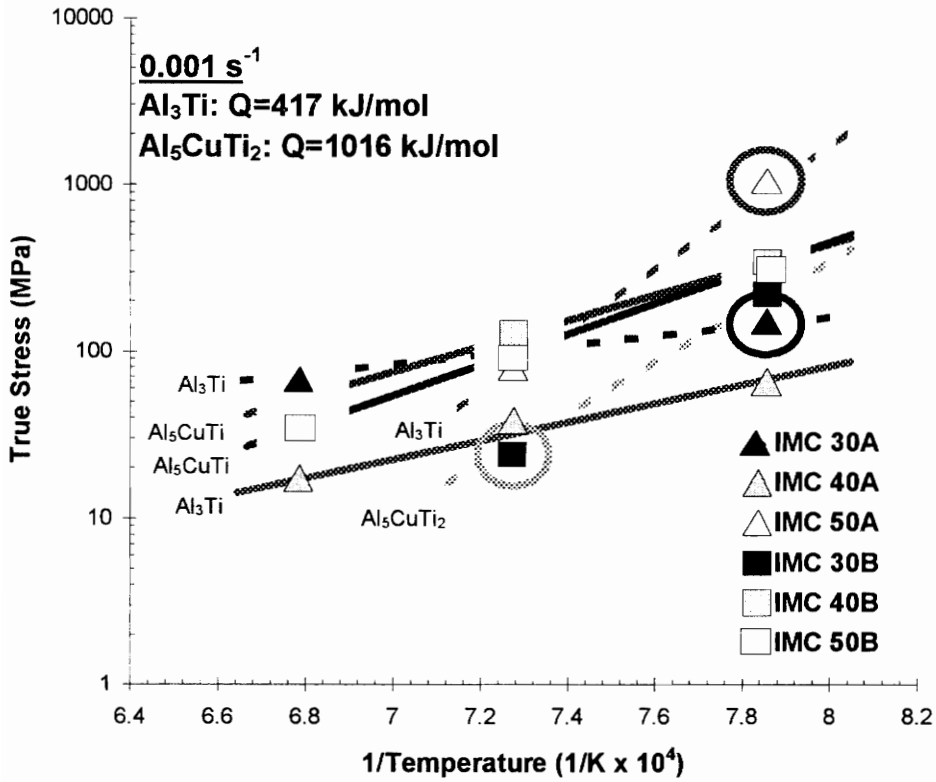


Figure 23: Plot of the true peak stress versus the inverse temperature on a log-linear scale for each of the composites at 0.001 s^{-1} . The slope of the trace of a trend line for each composition is that composite's activation energy. The circled points represent those not used in the calculations for activation energy due to temperature measurement errors.

Table XI: Activation energy values for each composite at each strain-rate.

Composite Designation ¹	Q (kJ/mol) 0.0001 sec ⁻¹	Q (kJ/mol) 0.001sec ⁻¹	Average over both strain-rates
IMC 30A ²	820	175	498
IMC 40A	526	511	519
IMC 50A	313	564	365
Average for all Al ₃ Ti's	553	417	485
IMC 30B ³	610	1,443	1,027
IMC 40B	815	793	804
IMC 50B	1,049	810	930
Average for all Al ₅ CuTi ₂ 's	825	1,016	920
Average for all composites	689	717	703

1. Example of composite designation: IMC 30A=Al₃Ti ("A" matrix) + 30 volume %TiB₂.
2. The average value for all Al₃Ti matrix composites, 0.349, was used to calculate Q for Al₃Ti + 30 volume % TiB₂.
3. The average value for all Al₅CuTi₂ matrix composites, 0.247, was used to calculate Q for Al₅CuTi₂ + 30 volume % TiB₂.

3.3.2.4. Structure Constant, A

The structure constant accounts for the variations in elastic constants, microstructures, volume fraction of reinforcement, and/or matrix composition not otherwise addressed directly in equation 3.1. Its values are determined for each composite variant after average strain-rate sensitivity and activation energies have been calculated. Table XIII shows the structure constant for each sample composition. No trends are discernable due to limited data.

Table XII: The structure constant as calculated for each composite.

Sample Designation	Structure Constant (MPa)
Al ₃ Ti + 30 vol% TiB ₂	3.28 x 10 ⁻⁴
Al ₃ Ti + 40 vol% TiB ₂	1.59 x 10 ⁻⁴
Al ₃ Ti + 50 vol% TiB ₂	2.87 x 10 ⁻⁴
Al ₅ CuTi ₂ + 30 vol% TiB ₂	7.84 x 10 ⁻⁷
Al ₅ CuTi ₂ + 40 vol% TiB ₂	1.32 x 10 ⁻⁶
Al ₅ CuTi ₂ + 50 vol% TiB ₂	1.27 x 10 ⁻⁶

4. DISCUSSION

4.1. Correlation of Microstructure to Mechanical Behavior

4.1.1. Effects of TiB_2 Reinforcement

The presence of TiB_2 in the composites does not greatly affect the flow behavior of these materials at high temperatures. The temperatures at which these compression tests were performed is very near the melting temperature of the matrix, and are comparable to temperatures in which conventional hot metal-working would be performed. As one would expect, at these temperatures the composite is extremely deformable, regardless of the reinforcement used. Therefore, the results of these mechanical tests have inherent scatter related to the extreme test temperatures and the resulting deformability of the matrix. The effects of the TiB_2 on the flow behavior of the composites then, are slight. To demonstrate this, the following sections will describe the flow behavior in terms of the interaction of TiB_2 particles with the matrix and with other TiB_2 particles.

4.1.1.1. Effect of Volume % on TiB_2 Size

Martin²⁸ presented a comparison of the average diameter of a TiB_2 particle within a TiAl matrix as a function of the adiabatic temperature obtained during synthesis of the

IMC's. Martin calculated the adiabatic temperature by assuming that all of the heat generated during the reaction synthesis is used to raise the temperature of the final products.³⁵ He found that the average TiB_2 particle diameter increased as a function of volume percent, and attributed this to an increase in the adiabatic temperature. Assuming that the adiabatic temperature of TiAl is similar to that of Al_3Ti and Al_5CuTi_2 , the composites of the present study should follow a similar trend. Figure 24 shows that this is not the case. As the adiabatic temperature increases (as a function of the volume % TiB_2), the average TiB_2 diameter increases in the sample reinforced with 40 volume % TiB_2 but then decreases for the samples reinforced with 50 volume %.

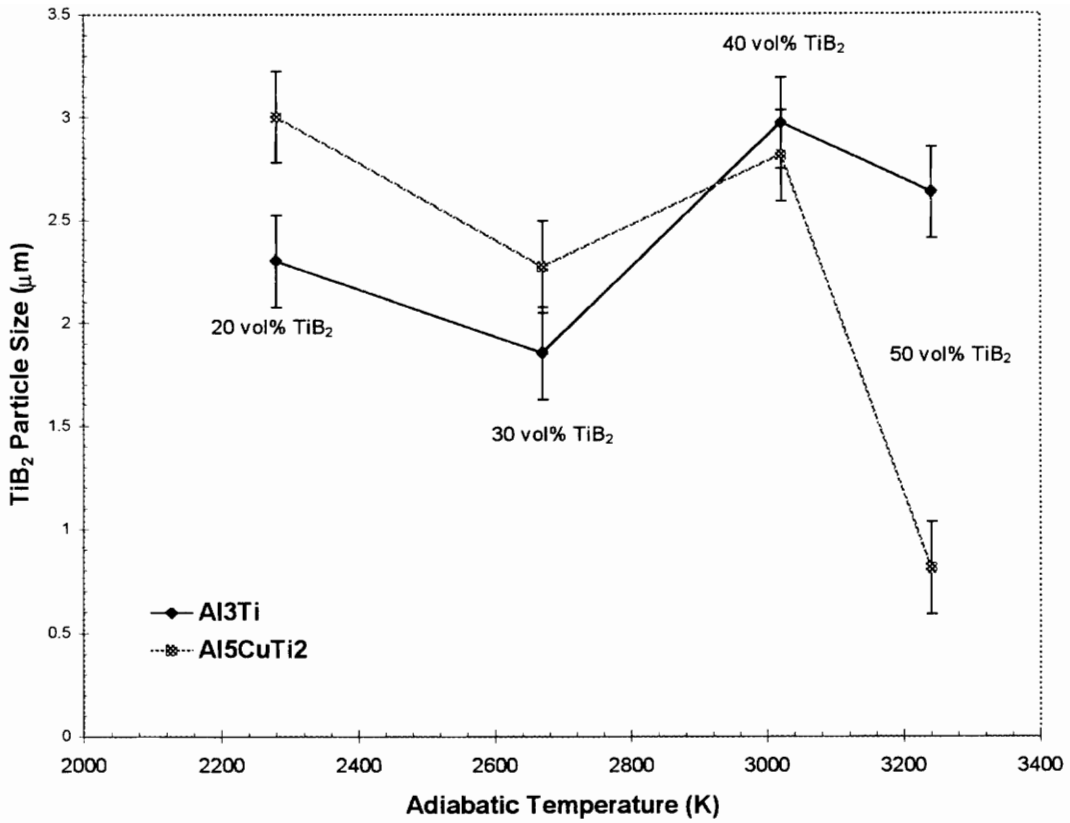


Figure 24: The TiB₂ equivalent particle diameter as a function of the adiabatic temperature.

4.1.1.2. Volume % TiB₂ Reinforcement

Figures 25-27 show the flow stress as a function of the volume % TiB₂ for each test temperature. The Al₃Ti-matrix composites go through a slight flow stress minimum at 40 volume % TiB₂. The Al₅CuTi₂-matrix composites go through a slight flow stress maximum at 40 volume % TiB₂ reinforcement. Normally, one would expect that the flow stress would increase with increasing volume % TiB₂ reinforcement. This would be the

case if the TiB_2 particulates were somehow acting as obstacles to dislocation motion. However, the trends which were observed seem to indicate that the flow behavior is dominated by matrix effects at these elevated temperatures. Therefore, the influence of TiB_2 might be expected to be limited to the effect they had on the matrix microstructure, i.e., grain size or compositional variation.

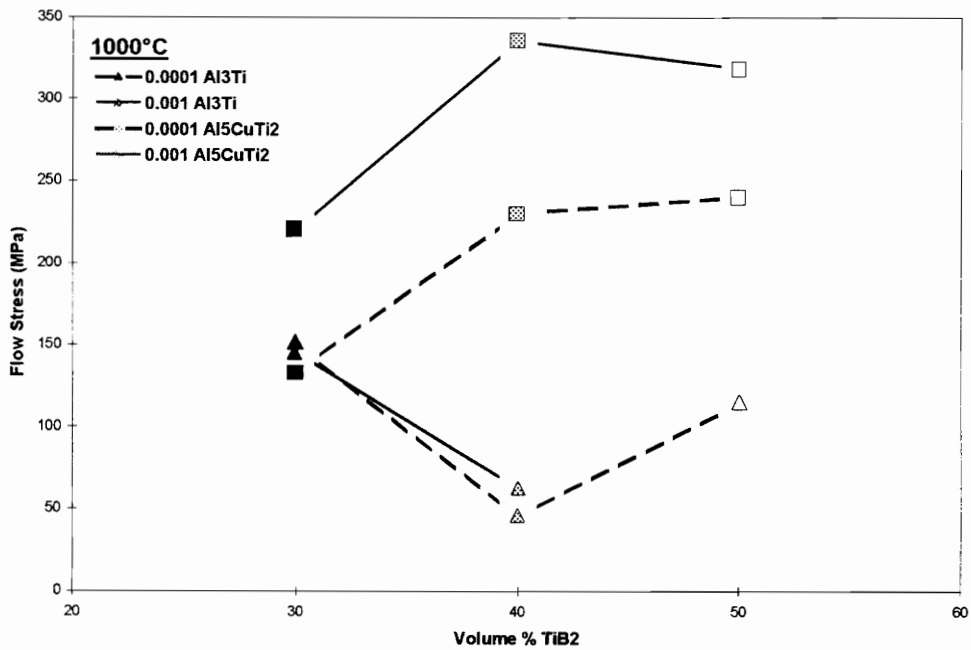


Figure 25: A comparison of flow stress as a function of volume % TiB_2 reinforcement at 1000°C.

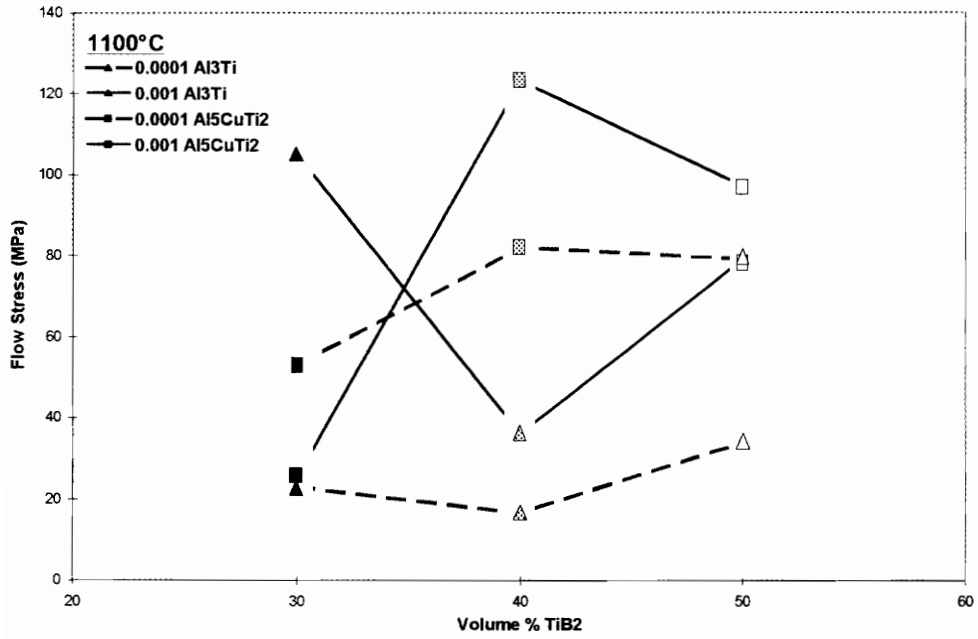


Figure 26: A comparison of flow stress as a function of volume % TiB₂ reinforcement at 1100°C.

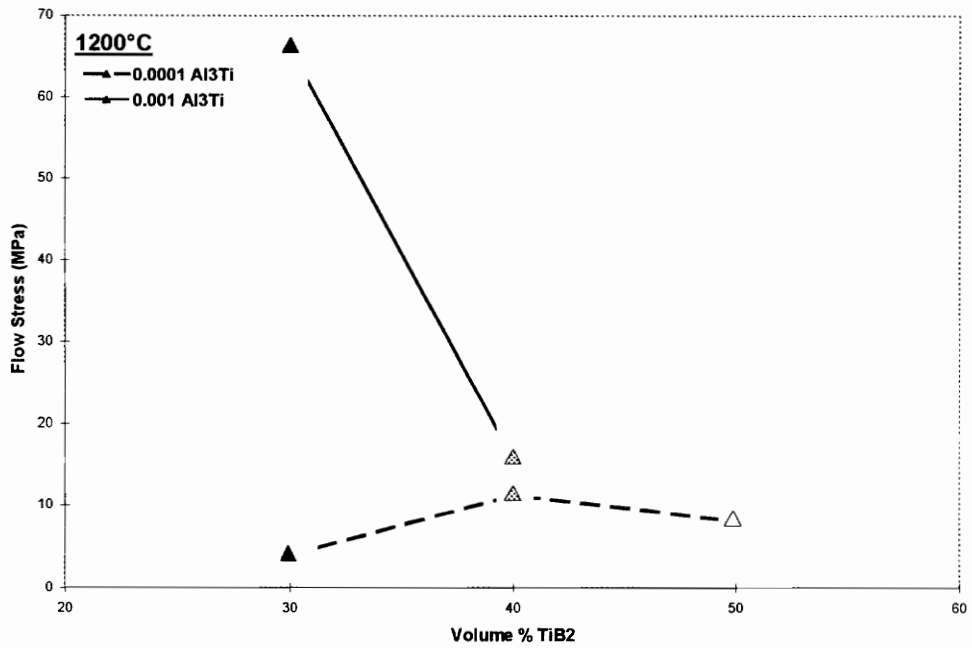


Figure 27: A comparison of flow stress as a function of volume % TiB₂ reinforcement at 1200°C.

4.1.1.3. TiB₂ particle size and interparticle spacing

One possible explanation for the variations, albeit slight, in flow stress observed for various volume fractions might be due to variations in spacing. Spacing relies strongly upon both volume fraction and average size. As presented previously, the interparticle spacing decreases with increasing volume fractions of TiB₂ and decreasing particle size, as expected.

4.1.1.4. Models of Dispersion Strengthening

To examine the possible influence of spacing of the dispersed TiB₂ on the observed flow behavior, one must identify the mechanism by which its influence occurs. Kampe et.al.,³ established an empirical relationship between flow stress and inverse-square-root of spacing for similar composite matrices, but at significantly lower volume fractions, and hence, much wider spacings. The $\sigma \propto \lambda^{-\frac{1}{2}}$ dependence, rather than the more familiar Orowan-based $\sigma \propto \lambda^{-1}$ relationship, was attributed to the relatively wide spacings present in these composites. However, the higher volume fractions and much smaller spacings measured in the composites of the present study increases the possibility that the more-potent Orowan mechanism may be operative. To test which is dominating, both dependencies of spacing on the flow stress is shown in Figure 28.

The Orowan Equation is normally used to describe the strength imparted by a dispersion strengthened alloy, in which the reinforcing particles are closely spaced. The

Hall-Petch relationship is usually used to describe the effect of grain size on an alloy.

Ideally, compression tests having the same temperature and strain-rates would yield flow stress data affected primarily by the volume fraction of the reinforcing phase, i.e., dispersion strengthening. It is apparent from the Figure 28 that conclusions cannot be drawn from the current pool of data.

4.1.2. Effect of the matrix composition on the mechanical behavior of the composites

The most prominent factor in the deformation of composites at temperatures very near the melting temperature of the matrices is the composition of the matrix. The composition affects the flow behavior by influencing both the magnitude of the thermally-activated contribution, as well as through significant microstructural differences.

4.1.2.1. Matrix composition and homologous temperature

The homologous temperature is a ratio of the test temperature to the melting temperature of a material. The homologous temperature for each of the composite matrices at each test temperature is shown in Table XIII.

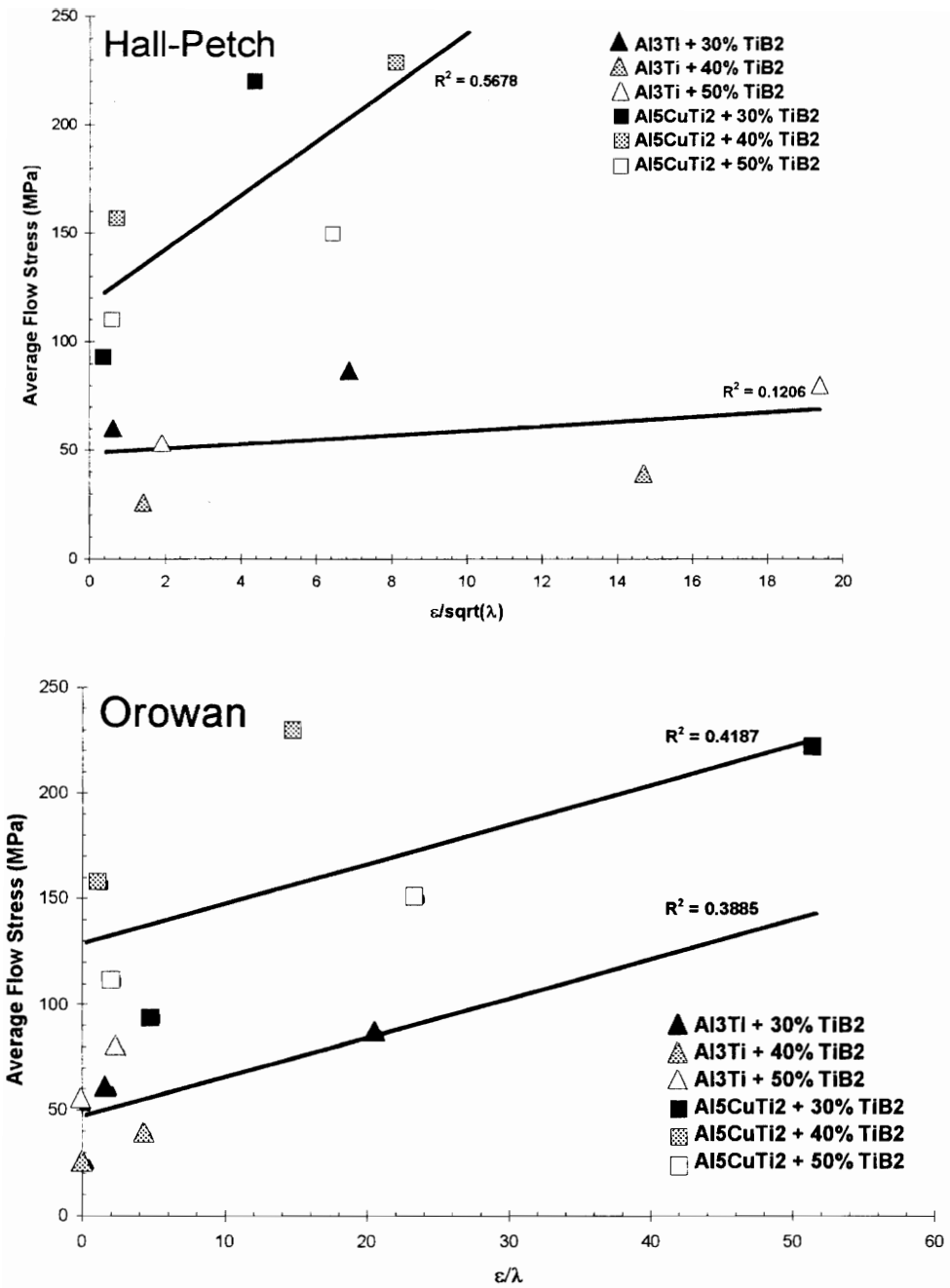


Figure 28: A comparison of flow stress as a function of interparticle spacing. The Hall-Petch model (top) describes the behavior of widely spaced particles. The Orowan model (bottom) shows the behavior of a composite with more finely dispersed particles.

Table XIII: The homologous temperature for each composite matrix at the specified test temperatures.

Temperature (K)	$T_{\text{homologous}}^{\text{Al}_3\text{Ti}}$	$T_{\text{homologous}}^{\text{Al}_5\text{CuTi}_2}$
1,273	0.78	0.78
1,373	0.84	0.85
1,473	0.9	0.91

Figure 29 shows the average flow stress as a function of the homologous temperature. In every case the flow stress decreases as the homologous temperature increases, as expected. However, the Al_5CuTi_2 -matrix composites should have strengths which are less than those of the Al_3Ti -matrix composites because of their higher homologous temperatures. This is not the case. This is most likely due to the unidentified basketweave structure encountered in the microstructural analysis. The presence of TiAl has been shown in the Al_3Ti -matrix composites. However, this method of analysis does not allow us to quantify the relative amounts of each phase within the matrix. It is assumed that since the temperature of the reaction synthesis, i.e., the adiabatic temperature, increases proportionally to the volume % TiB_2 , the amount of aluminum lost to volatilization during the reaction synthesis also increases. This aluminum volatilization greatly affects the composition of the matrix.

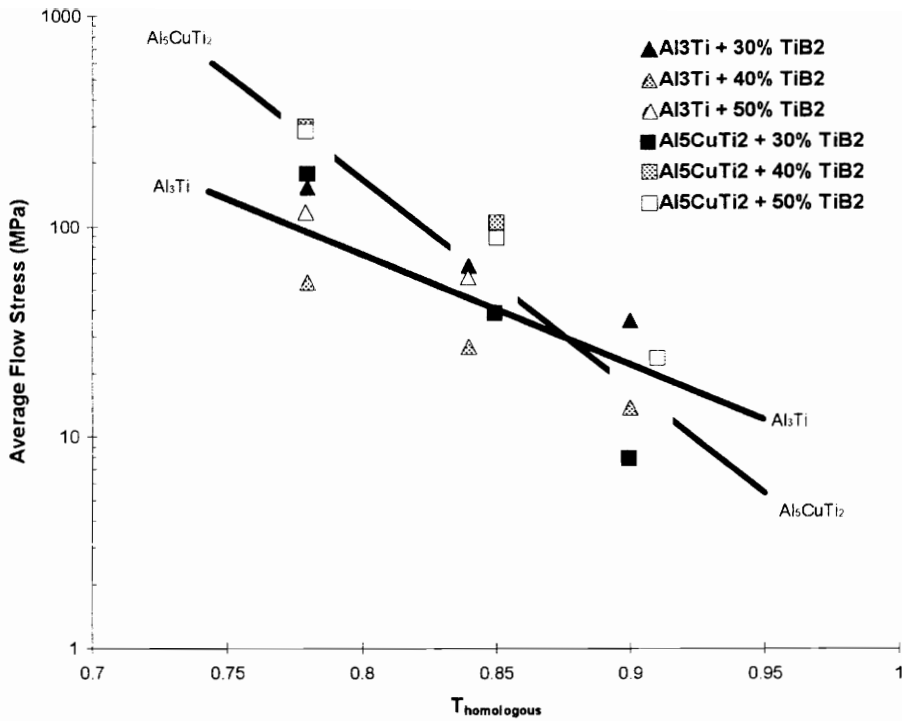


Figure 29: A plot of the average flow stress as a function of the homologous temperature.

4.2. Development of Constitutive Equations

4.2.1. The Zener-Hollomon Parameter

The Zener-Hollomon Parameter³⁴, or temperature compensated strain rate, allows the effects of strain rate and temperature to be combined into one variable. This parameter is defined as:

$$Z = \dot{\epsilon} \exp\left(\frac{Q}{RT}\right) \quad \text{Equation 4-1}$$

Sellars and Tegart^{36,37} also proposed a method for correlating stress, temperature, and strain rate:

$$\dot{\epsilon} = A(\sinh \alpha\sigma)^m \exp\left(\frac{-Q}{RT}\right) \quad \text{Equation 4-2}$$

where α is related to the activation volume³⁸. If we assume that $\alpha=0.001$, then plotting $\sinh(\alpha\sigma)$ as a function of the Zener-Hollomon Parameter on a log-log scale, reveals a series of parallel lines of constant strain rate and temperature. This is clearly evident in Figure 30. The information contained in this plot is fundamental to the codeformation processing foreseen as a potential application of this research.

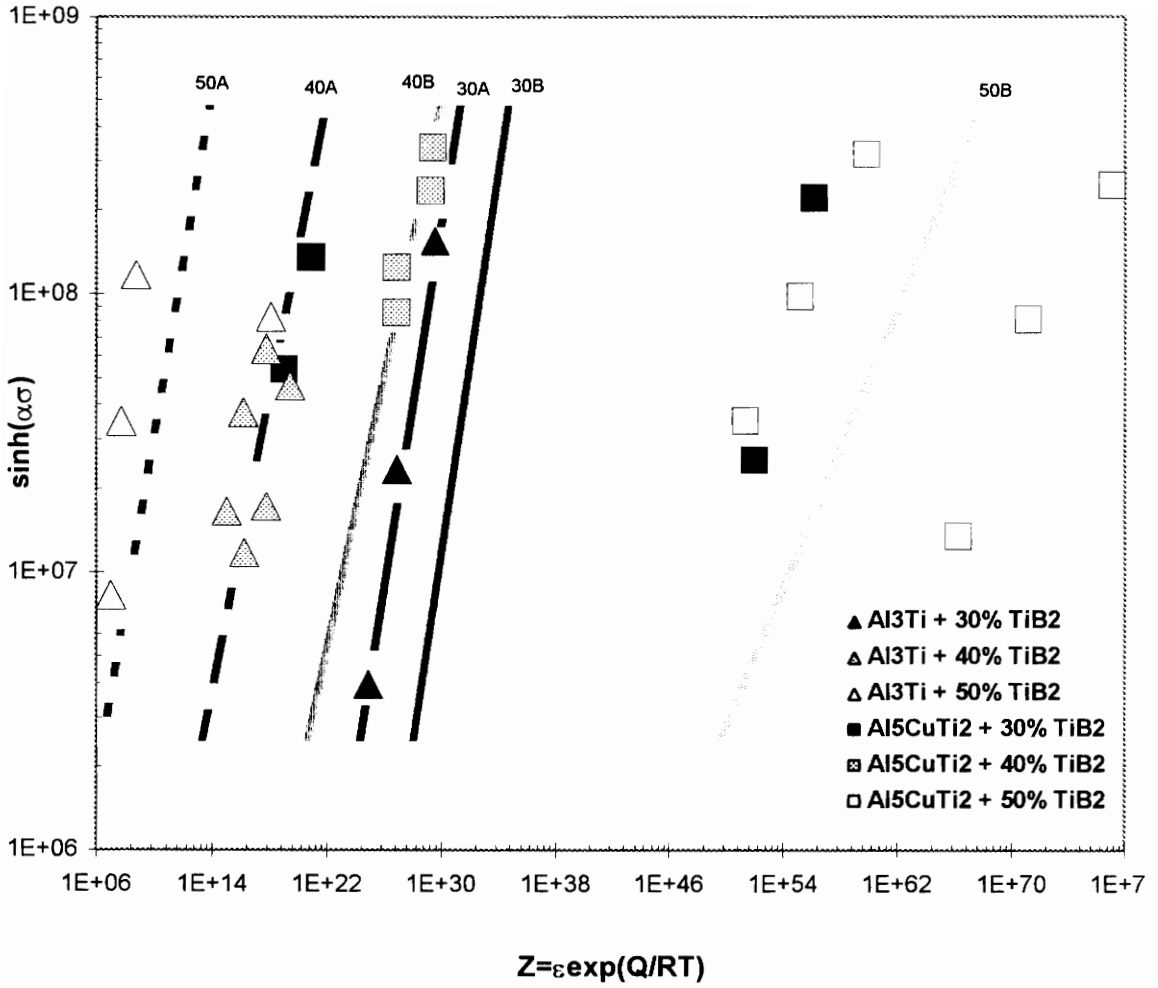


Figure 30: The peak flow stress as a function of the Zener-Hollomon Parameter. The parallel lines represent lines of constant strain rate and temperature.

4.2.2. Constitutive Flow Stress Equations

The development of phenomenologically-based constitutive equations to describe the flow stress of these composites as a function of strain rate and temperature requires the determination of the activation energy (Q), strain-rate sensitivity (m), and the structure constant (A). Analysis of the true stress peaks of the compression testing was used to calculate these values.

The activation energy appears to be nearly constant for each matrix composition over the range of temperatures and strain-rates tested. This suggests that all deformation occurs within the intermetallic matrix. Further, this implies that the scatter in the activation energy values is solely due to variations within the intermetallic matrix, as observed in microstructural and x-ray diffraction analysis. The relative constancy of the activation energy values suggests that it is appropriate to average the values for each matrix variant for its use in a generalized constitutive equation. The average activation energies so determined in section 3.3.2.3, and used in the constitutive equations, are 485 kJ/mol and 920 kJ/mol for the Al_3Ti and Al_5CuTi_2 matrices, respectively.

The degree of scatter in the observed strain-rate sensitivities is more difficult to quantify. This scatter is undoubtedly tied to the difficulties involved in testing at these high temperatures and is further affected by the limited data available. In an effort to minimize the effects of this variation, an average value will be determined for use in the constitutive equation for each matrix composition. These values, as calculated in section

3.3.2.2, are 0.349 for the Al₃Ti-atrix composites and 0.247 for the Al₅CuTi₂-based composites.

The structure constant, assumed to be independent of both strain rate and temperature, must be recalculated for these average values. The re-calculated structure constants are shown in tabular form with the average strain-rate sensitivities and activation energies in Table XIV. These are the components used in the development of an average or generalized constitutive flow stress equation, originally given as equation 3-2; as shown below.

$$\sigma_{flow} = A \cdot \dot{\epsilon}^m \cdot \exp\left(\frac{mQ}{RT}\right)$$

Table XIV: The structure constants, strain-rate sensitivities, and activaton energies utilized in the flow stress equation-based constitutive equations.

Sample Composition	Structure Constant, A (MPa)	Strain-rate Sensitivity, m	Activation Energy, Q (kJ/mol)
Al ₃ Ti + 30 vol% TiB ₂	3.28 x 10 ⁻⁴	0.349 ¹	485 ³
Al ₃ Ti + 40 vol% TiB ₂	1.59 x 10 ⁻⁴		
Al ₃ Ti + 50 vol% TiB ₂	2.87 x 10 ⁻⁴		
Al ₅ CuTi ₂ + 30 vol% TiB ₂	7.84 x 10 ⁻⁷	0.247 ²	920 ⁴
Al ₅ CuTi ₂ + 30 vol% TiB ₂	1.32 x 10 ⁻⁶		
Al ₅ CuTi ₂ + 30 vol% TiB ₂	1.27 x 10 ⁻⁶		

1. Average value of strain-rate sensitivity for Al₃Ti-matrix composites
2. Average value of strain-rate sensitivity for Al₅CuTi₂-matrix composites
3. Average value of activation energy for Al₃Ti-matrix composites
4. Average value of activation energy for Al₅CuTi₂-matrix composites.

Figures 31-36 show plots of the flow stress as a function of both the temperature and strain rate. These plots indicate that the flow behavior of these composites is strongly temperature dependent, with relatively moderate strain-rate sensitivity. The influence of the strain rate increases with decreasing temperature. Similarly, although not as dramatically, the influence of temperature on the flow behavior increases with increasing strain rate. This trend is consistent in all composite variants.

The average correlation of these constitutive equations is 25%. The best fit occurred in the samples reinforced with 50 volume % TiB_2 . The Al_3CuTi_2 -matrix composites had better correlation than the Al_3Ti -matrix composites.

The correlation values allow for a semi-quantitative evaluation of the use of an average strain-rate sensitivity and activation energy for each composite. Although these values are not independent, some general statements can be made regarding whether each should be increased or decreased to accommodate better correlation of the constitutive equations to the actual material response. For instance, by increasing the strain-rate sensitivity value for the $\text{Al}_3\text{Ti} + 30$ volume % TiB_2 from 0.349 to 0.356, the correlation improves from 65.9% to 80.6%. Similarly, in the $\text{Al}_3\text{CuTi}_2 + 30$ volume % TiB_2 , by adjusting the activation energy from 920 kJ/mol to 907 kJ/mol, an improvement of 24.6% (i.e., from 66.7% to 91.3%) can be achieved. Greater improvements are possible by maximizing both the strain-rate sensitivity and the activation energy. Changes in any one of the values used in the constitutive equation can greatly effect the maximization of the remaining two variables due to the complex relationship interactions of A , m , and Q . This

is another advantage in the application of the average m and Q values for each composite.

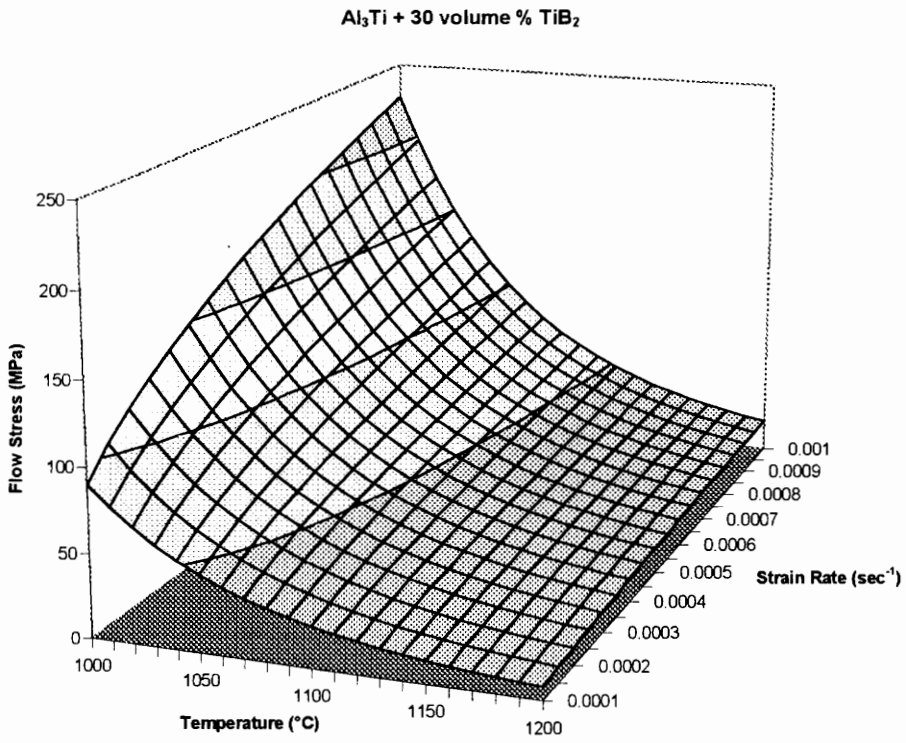


Figure 31: A plot of the flow stress as a function of the temperature and strain rate for Al₃Ti + 30 volume % TiB₂.

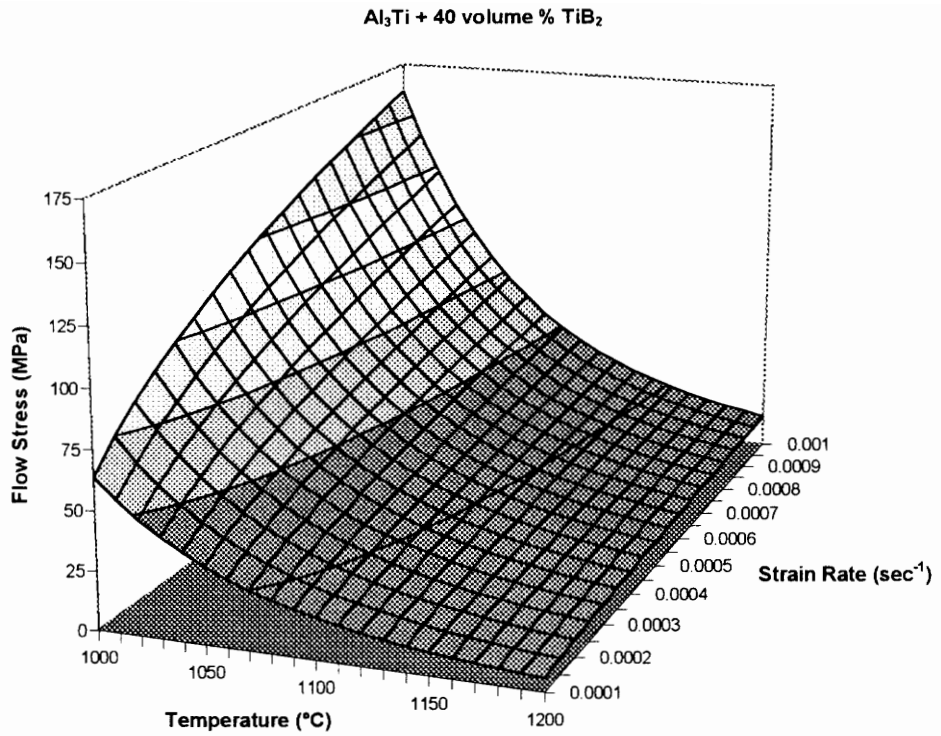


Figure 32: A plot of the flow stress as a function of the temperature and strain rate for Al₃Ti + 40 volume % TiB₂. It correlates very well to the measured flow stresses.

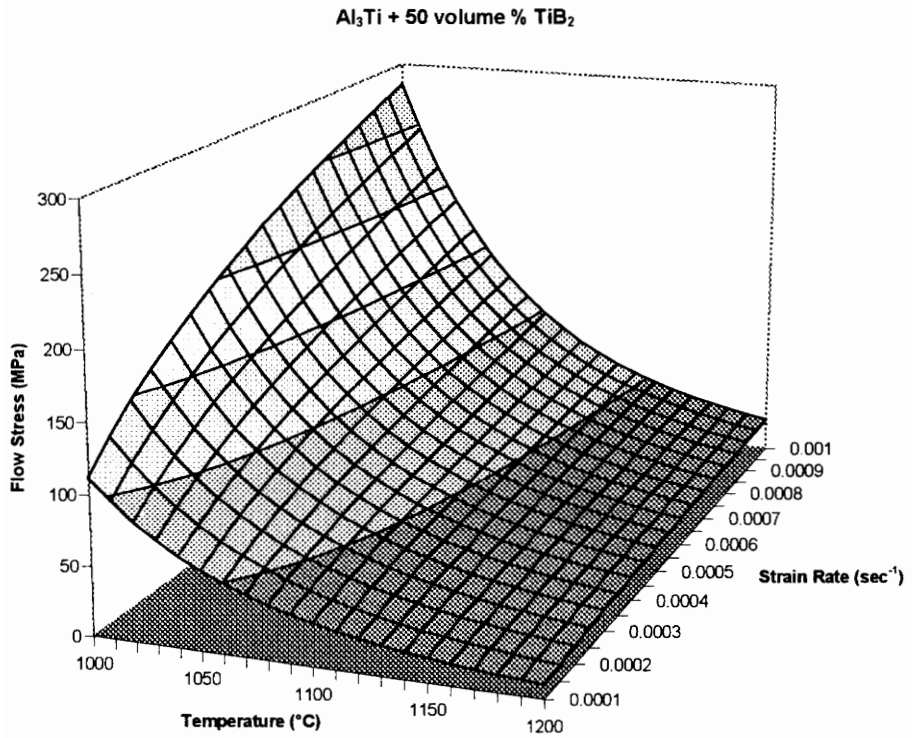


Figure 33: A plot of the flow stress as a function of the temperature and strain rate for Al₃Ti + 50 volume % TiB₂.

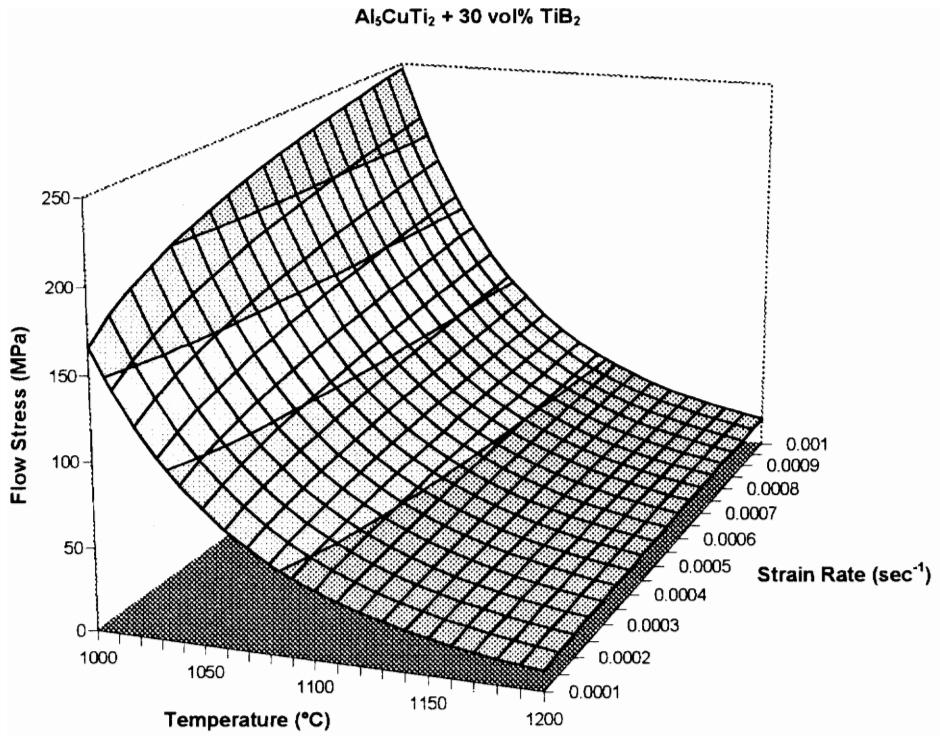


Figure 34: A plot of the flow stress as a function of the temperature and strain rate for Al₅CuTi₂+ 30 volume % TiB₂.

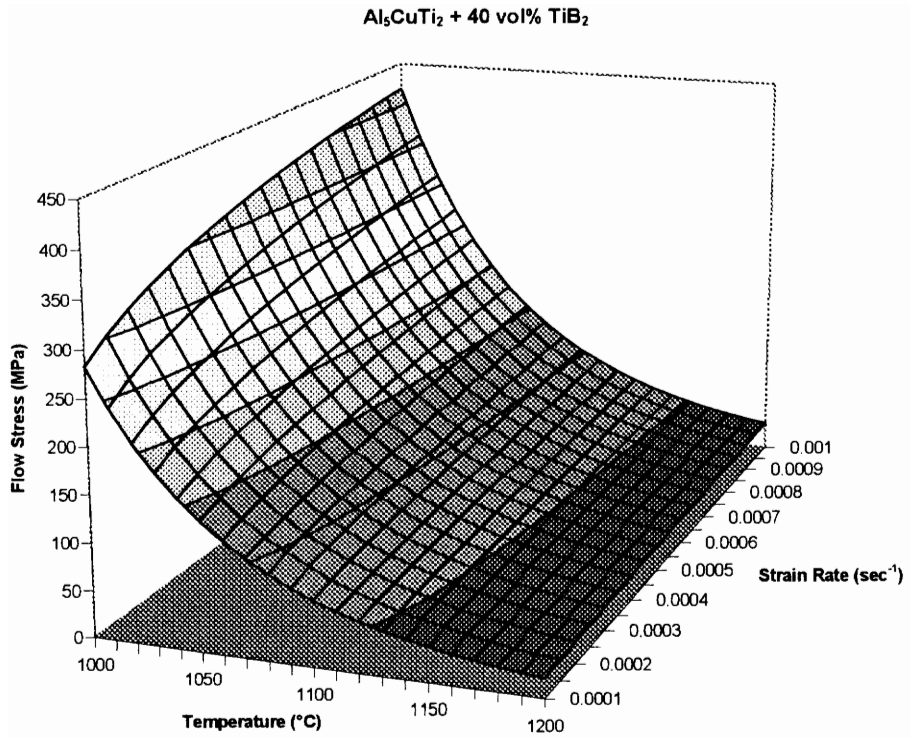


Figure 35: A plot of the flow stress as a function of the temperature and strain rate for $\text{Al}_5\text{CuTi}_2 + 40 \text{ volume } \% \text{TiB}_2$.

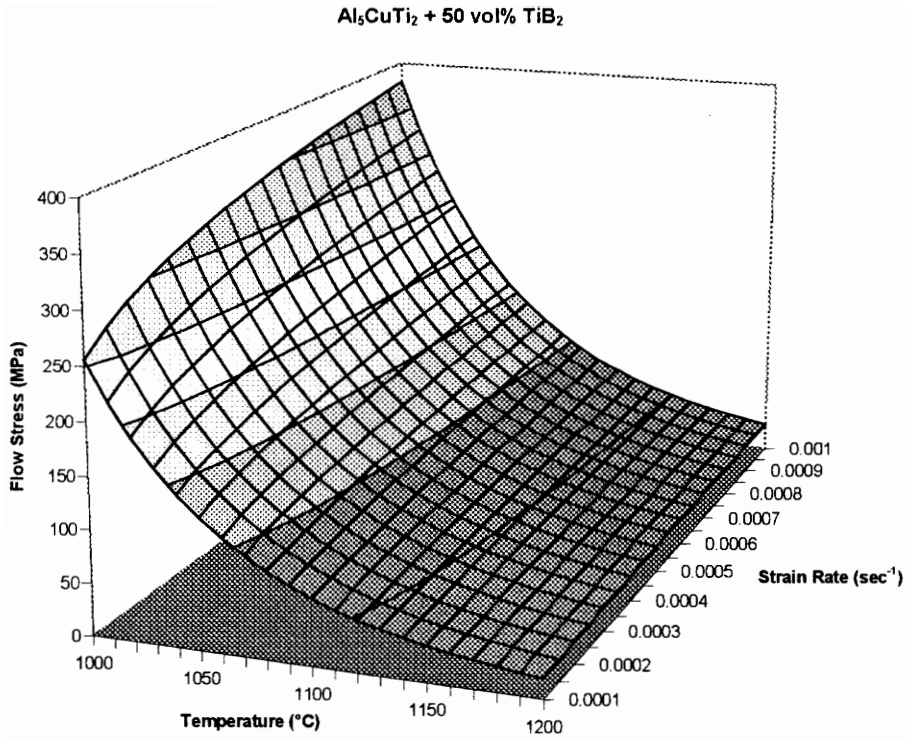


Figure 36: A plot of the flow stress as a function of the temperature and strain rate for $\text{Al}_3\text{CuTi}_2 + 50 \text{ volume } \% \text{ TiB}_2$.

4.3. Future Work and Potential Applications

4.3.1. Application to other intermetallic matrix composites

The approach utilized in this study has also been applied to studies involving TiAl + TiB₂ and Al₂Cu + TiB₂. Table XV is a list of potential intermetallic matrices and reinforcements which could be prepared using the reaction synthesis techniques described in this study.

Table XV: A list of potential intermetallic matrices and reinforcements.^{2,4}

Potential Composites
NiAl + TiB ₂
(NiAl+Ni ₂ AlTi) + TiB ₂
CoAl + TiB ₂
(TiAl +Ti ₃ Al) + B ₄ C
Al ₃ Nb + TiB ₂
Al ₂ Cu + TiB ₂
MoSi ₂ + SiC
FeAl + Fe ₃ C

4.3.2. Codeformation Processing

The initial motivation behind this research lies in the development of constitutive equations able to be used as models to "dial in" flow stresses as a function of temperature and strain rate. These composites could be used as the reinforcing phase in a titanium

alloy matrix composite. Further, elongated morphologies could be achieved by equalizing the flow stresses within the IMC and the titanium matrix material. During a coextrusion process, for example, the point at which the Zener-Hollomon lines cross for two materials indicate a point at which the materials achieve equal flow stress when at the same strain rate and temperature, thus achieving the desired IMC reinforcement morphology.

4.4. Summary and Conclusions

4.4.1. Summary

Al₃Ti-, Al₅CuTi₂-, and Al₆₆Mn₁₁Ti₂₃-matrix composites reinforced with 30, 40, and 50 volume % TiB₂ dispersed ceramic particulate have been successfully reaction synthesized from elemental powders. The as-reacted composite sponges were reduced into a fine powder, encapsulated, and HIPed to produce solid right cylinders. Compression samples were sectioned from these cylinders and tested at 1000°, 1100°, and 1200°C at strain rates of 0.0001 sec⁻¹ and 0.001 sec⁻¹. The peak flow stresses from these tests were recorded and used to calculate the strain-rate sensitivity and the activation energy.

The microstructure of each composite was also evaluated. The microstructure was analyzed in terms of the matrix composition, the volume % dispersed reinforcement, and

the size and interparticle spacing of the reinforcement. These microstructural features were correlated to the high temperature mechanical flow response of the composites.

Constitutive equations were developed based upon the flow stress equation. The structure constant, strain-rate sensitivity, and activation energy were determined, as they were fundamental to the constitutive equation. A modification of this approach to describing the flow stress was applied to incorporate the strain rate and temperature into one variable: the Zener-Hollomon Parameter.

4.4.2. Conclusions

- The synthesis of titanium aluminide matrix composites reinforced with high loadings of dispersed ceramic reinforcement from elemental powder is readily accomplished using XD™ synthesis techniques. However, aluminum volatilization during synthesis complicates the prediction of the exact composition of the matrix, resulting in the formation of a multiphase matrix alloy.
- The interparticle spacing of the TiB₂ reinforcement decreases with increasing volume % of reinforcement and decreasing particle size, as expected.
- The effect of dispersion strengthening by the TiB₂ in these composites was evaluated to determine the mechanism by which any reinforcement-related strengthening occurred at these temperatures. It was found that further testing will be required to specify a mechanism of dispersion strengthening.

- Flow in these composites occurs strictly within the matrix material. This is substantiated by the lack of TiB_2 -dependent behavior with variations in volume percentage of reinforcement. The flow behavior in these composites, then, is more a function of matrix composition than the presence of TiB_2 . In all cases, the composites are readily deformed at relatively low loads.
- The development of constitutive equations to describe the behavior of these materials in terms of the effect of strain rate and temperature on the flow stress revealed that the flow behavior of the composites is highly dependent on matrix composition and temperature. The effects of strain rate are not evident at higher temperatures but appear to affect limited influence at the lower test temperatures.
- The Zener-Hollomon Parameter offers a convenient technique for combining the temperature and strain rate into a single variable, thereby allowing the flow stress to be plotted along lines of constant temperature and strain rate. The as-measured flow stresses were consistent with these lines.
- According to these constitutive equations, the codeformation of these composites as a reinforcing phase in a metal matrix composite will allow for the formation of novel reinforcement morphologies.

REFERENCES

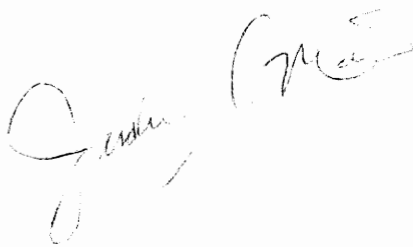
1. S.L. Kampe, "Feasibility of (IMC)_d-reinforced metal matrix composites", *Final Technical Report to ONR contract # N00014-93-1-0539*, (1994).
2. K. Sharvan Kumar, "Review: Discontinuously Reinforced Intermetallic Matrix Composites", *ISIJ International* vol. 31, no. 10, pp.1249-59, (1991).
3. S.L. Kampe, P.Sadler, L. Christodoulou & D.E. Larsen, "Room-temperature Strength and Deformation of TiB₂-Reinforced Near- γ Titanium Aluminides", *Met. Trans A*, vol. 25A, pp.2181-97, (1994).
4. K.S. Kumar and J.D. Whittenberger, "Discontinuously Reinforced Intermetallic Matrix Composites via XD[®] Synthesis", *Mat Sci Tech*, vol. 8, pp.317-30, (1992).
5. J.M. Kampe "Multilithic Metal Matrix Composites", *SBIR Proposal #94-104.08 5082 A*, (1994).
6. J.C. Beddoes, W. Wallace & M.C. Mahlerbe, "The Technology of Titanium Aluminides for Aerospace Applications", *Mater Man Proc.* vol. 7, no. 4, pp.527-59, (1992).
7. D.M. Dimiduk, D.B. Miracle, Y-W. Kim & M.G. Mendiratta, "Review: Recent Progress in Intermetallic Alloys for Advanced Aerospace Systems", *ISIJ International*, pp.1223-34, (1991).
8. C.R. Kachelmyer & A. Varma, "Combustion Synthesis of Niobium Aluminide Matrix Composites", *Mat Res Soc Symp Proc*, vol. 350, pp. 33-9, (1994).
9. D.E. Alman, J.A. Hawk, C.P. Dogan, M. Ziomek-Moroz & A.V. Petty, Jr., "Microstructure and Properties of Intermetallic Matrix Composites Produced by Reaction Synthesis", *Mat Res Soc Symp Proc*, vol. 350, pp. 25-31, (1994).
10. M.E. Hyman, C. McCullough, J.J. Valencia, C.G. Levi & R. Mehrabian, "Microstructure Evolution in TiAl Alloys with B Additions: Conventional Solidification", *Met Trans A*, vol. 20A, pp. 1847-59, (1989).
11. F.H. Froes, C. Suryanarayana & D. Eliezer, "Production, Characteristics, and Commercialization of Titanium Aluminides", *ISIJ International*, vol. , pp. 1235-48, (1991).
12. F.H. Froes, C. Suryanarayana & D. Eliezer, "Review: Synthesis, Properties and Applications of Titanium Aluminides", *J Mat Sci*, vol. 27, pp. 5113-40, (1992).
13. C.R. Feng, H.H. Smith, D.J. Michel & C.R. Crowe, "Microstructure of XD[™] Titanium Aluminides", in *Microstructure Property Relationships in*

- Titanium Aluminides and Alloys*, ed. Y-W Kim and R.R. Boyer, TMS, pp. 353-9, (1991).
14. A.B. Pandey, R.S. Mishra & Y.R. Mahajan, "High-temperature Creep of Al-TiB₂ Particulate Composites", *Mat Sci & Eng*, vol A189, pp. 95-104 (1994).
 15. *Binary Alloy Phase Diagrams*, edited by T.B. Massalski, ASM, Metals Park, Ohio, vol. 1, p. 104, (1986).
 16. L. Wu, D. Pope & V. Vitek, "Deformation and Fracture of L1₂ (Al,Fe)₃Ti", *Scr Met*, vol. 24, pp.2187-90, (1990).
 17. K.S. Kumar and J.R. Pickens, "Compression Behavior of the L1₂ Intermetallic Al₂₂Fe₃Ti₈", *Scr Met*, vol. 22, pp. 1015-18, (1988).
 18. S. Zhang, J.P. Nic, W.M. Milligan & D.E. Mikkola, "Temperature Dependence of the Compressive Strength of Cubic Phases Formed by Alloying Al₃Ti with Mn and Cr", *Scr Met*, vol. 24, pp.1441-6, (1990).
 19. X. Chen, X. Wu, W.L. Fang, S. Chen & G. Hu, "The Role of Hot-working on the Microstructure and Mechanical Properties of the L12-type Mn Modified Al₃Ti Alloy", *Mat Sci Eng*, vol. A153, pp. 370-6, (1992).
 20. X. Chen, X. Wu, S. Chen & G. Hu, "Ductility Improvement on Al₆₇Ti₂₅Mn₈ Intermetallic Alloy Via Hot-Working", *Scr Met*, vol. 26, pp.1775-8, (1992).
 21. M. Yamaguchi, Y. Umakoshi & T. Yamane, "Plastic Deformation of the Intermetallic Compound Al₃Ti", *Phil Mag A*, vol. 55, no. 3, pp.301-15, (1987).
 22. I Barin, et.al., *Thermochemical Data of Pure Substances, 2nd ed.*, VCH, Weinheim, Germany, 1989.
 23. J. Tarnacki and Y-W. Kim, "A Study of Rapidly Solidified Al₃Ti Intermetallics with Alloying Additions", *Scr Met*, vol. 22, pp. 329-34, (1988).
 24. I. Barin, *Thermochemical Properties of Inorganic Substances by I. Barin and O. Knacke*, Springer-Verlag, Berlin, Germany, (1973).
 25. D.A. Porter and K.E. Easterling, *Phase Transformations in Metals and Alloys*, Van Nostrand Reinhold (International), p. 366, (1988).
 26. J. Subrahmanyam and M. Vijayakumar, "Review: Self-Propagating High-Temperature Synthesis", *J Mat Sci*, vol. 27, pp. 6249-73, (1992).
 27. A.G. Merzhanov, *Fizik. Khim. Soverem. Problem.*, p. 7, (1983).
 28. R. Martin, Master's Thesis, Virginia Polytechnic Institute and State University, Fall 1994.
 29. T. Pete, Master Thesis, Virginia Polytechnic Institute and State University, Fall 1994.

30. Kampe, et.al., "XDTM-derived Discontinuously-Reinforced Composites"
31. ASTM Standard Designation B 214-92, "Standard Test Method for Sieve Analysis of Granular Metal Powders", pp. 49-51, (1992).
32. J.W. Martin, *Micromechanisms in Particle-hardened Alloys*, Cambridge Solid State Science Series, p. 44., (1979).
33. M. Asta, D. de Fontaine & M. van Schilfgaard, "First-principles Study of Phase Stability of Ti-Al Intermetallic Compounds", *J Mat Res*, vol. 8, no. 10, pp. 2554-68, (1993).
34. C. Zener & H.H. Hollomon, *J Appl Phys*, vol. 15, pp. 22-32, (1944).
35. W.L. Frankenhouse, K.W. Brendley, M.C. Kieszek & S.T. Sullivan, *Gasless Combustion Synthesis of Refractory Compounds*, Noyes Publications. Park Ridge, p. 52, (1985).
36. C.M. Sellars & W.J. McG. Tegart, *Mem Sci Rev Metall*, vol 63, p. 731, (1966)
37. W.J.McG. Tegart, "Ductility", *ASM Handbook*, chap. 5, Metals Park, OH, (1968).
38. S.L. Kampe, personal communication.

VITA

Judson Sloane Marte was born in Philadelphia, Pennsylvania on May 25, 1971. He was raised in suburban Langhorne, Pennsylvania where he attended the Holy Ghost Preparatory School. Upon graduation from Holy Ghost in 1989, he left to pursue a degree in Materials Science and Engineering at the Johns Hopkins University's Whiting School of Engineering. Before graduating, he was advised by Dr. Dennis Nagle to pursue graduate study at Virginia Tech under the tutelage of Dr. Stephen L. Kampe. After earning his Bachelor of Science degree in 1993 he left to join Virginia Tech's Materials Science and Engineering Department. This marked the beginning of a period of intense academic growth. At Virginia Tech, he has spent the past 3 years dodging equipment failures and travelling while finishing the first stage of his research on titanium aluminide matrix composites. He intends to continue his investigation of metallic and intermetallic matrix composites as he works toward his doctoral degree.

A handwritten signature in black ink, appearing to read "Judson Marte", is written in a cursive style.